As of 10 June 2016

This GOES-R Level 2+ space weather Algorithm Theoretical Basis Document (ATBD) is preliminary and subject to change as the GOES-R Program prepares for a launch in late 2016.

The NOAA National Centers for Environmental Information (NCEI) is currently developing a demonstration version of the Satellite Product Analysis and Distribution Enterprise System (SPADES) which will host the L2+ algorithms. The operational SPADES will be instantiated by the National Weather Service in FY2017 to serve the needs of the Space Weather Prediction Center (SWPC).

Updated versions of the L2+ ATBDs will periodically be made available and posted to the SPADES website.

Bill Denig
NCEI

http://www.ngdc.noaa.gov/stp/space-weather/online-publications/stp_sii/spades/

# NOAA NESDIS
# National Geophysical Data Center

## GOES-R SEISS.20
## SOLAR ENERGETIC PARTICLE EVENT
## LINEAR ENERGY TRANSFER
## ALGORITHM THEORETICAL BASIS
## DOCUMENT
## Version 1.2

Hardcopy Uncontrolled

TITLE: SEISS.20 SOLAR ENERGETIC PARTICLE EVENT LINEAR ENERGY TRANSFER ALGORITHM THEORETICAL BASIS DOCUMENT VERSION 1.1

AUTHORS:
Juan V. Rodriguez

APPROVAL SIGNATURES:

_____ <Actual Signature Date>
Terrance G. Onsager
SEISS Instrument Scientist

_____ <Actual Signature Date>
William Denig
NGDC Principal Investigator

_____ <Actual Signature Date>
Steven Goodman
GOES-R Chief Scientist

SEISS.20 SOLAR ENERGETIC PARTICLE EVENT LINEAR ENERGY TRANSFER
ALGORITHM THEORETICAL BASIS DOCUMENT
VERSION HISTORY SUMMARY

| **Version Number** | **Date** | **Authors** | **Revision Description** | **Reason for Revision** |
|---|---|---|---|---|
| 1.0 | June 7, 2013 | Juan V. Rodriguez | Initial release | CDR |
| 1.1 | January 2, 2014 | Juan V. Rodriguez | Requirements moved from 3.1 to Appendix A. Title, signature pages, headers reformatted. | External peer review |
| 1.2 | May 20, 2014 | Juan V. Rodriguez | Updated Figure 2 and new figures showing results with 100 and 500 mil Al. Small changes, corrections, and clarifications resulting from science code completion. | Science code completion |

TABLE OF CONTENTS

LIST OF FIGURES ..... 8
LIST OF TABLES ..... 10
LIST OF ACRONYMS ..... 11
ABSTRACT ..... 12
1.0 INTRODUCTION ..... 13
1.1 Purpose of This Document ..... 13
1.2 Who Should Use This Document ..... 13
1.3 Inside Each Section ..... 13
1.4 Related Documents ..... 14
1.5 Revision History ..... 14
2.0 OBSERVING SYSTEM OVERVIEW ..... 15
2.1 Product Generated ..... 15
2.2 Instrument Characteristics ..... 16
3.0 ALGORITHM DESCRIPTION ..... 17
3.1 Algorithm Overview ..... 17
3.2 Processing Outline ..... 17
3.3 Algorithm Input ..... 17
3.3.1 Primary Data ..... 17
3.3.2 Ancillary Data ..... 18
3.4 Theoretical Description ..... 18
3.4.1 Physics of the Problem ..... 18
3.4.2 Mathematical Description ..... 21
3.4.3 Algorithm Output ..... 31
4.0 TEST DATA SETS AND OUTPUTS ..... 34
4.1 Simulated/Proxy Input Data Sets ..... 34
4.2 Test Results Using Proxy Input Data ..... 34
5.0 PRACTICAL CONSIDERATIONS ..... 47
5.1 Numerical Computation Considerations ..... 47
5.2 Programming and Procedural Considerations ..... 47
5.3 Quality Assessment and Diagnostics ..... 47
5.4 Exception Handling ..... 47
5.5 Algorithm Validation ..... 47
6.0 ASSUMPTIONS AND LIMITATIONS ..... 48
6.1 Constants to be Re-evaluated During Cal/Val ..... 48
6.2 Input and Output File Contents and Formats ..... 48
6.3 Performance ..... 48
6.4 Pre-Planned Product Improvements ..... 48
7.0 REFERENCES ..... 48
APPENDIX A. REQUIREMENTS. ..... 52
APPENDIX B. UNITS OF LET AND SHIELDING ..... 53

**LIST OF FIGURES**

Figure 1. Lorentz factor γ for EHIS channels E1 and E5 as a function of the heavy ion atomic number. (CDR estimates.) ..... 16
Figure 2. Electronic mass stopping power (Sele/ρ) in silicon of the most abundant heavy ions in solar energetic particle events, below the maximum EHIS energy (by species). From SRIM PRAL [Ziegler et al., 2008]. ..... 20
Figure 3. Look-up tables LUT1 (energy degradation) and LUT2 (flux degradation) for energies appropriate to 50 mil aluminum shielding and the nine projectile species included in the real-time LET algorithm. ..... 24
Figure 4. Look-up tables LUT1 (energy degradation) and LUT2 (flux degradation) for energies appropriate to 100 mil aluminum shielding and the nine projectile species included in the real-time LET algorithm. ..... 25
Figure 5. Look-up tables LUT1 (energy degradation) and LUT2 (flux degradation) for energies appropriate to 500 mil aluminum shielding and the nine projectile species included in the real-time LET algorithm. ..... 26
Figure 6. Maximum flux spectra for the 22 largest SEP events in Solar Cycle 23 for (clockwise from upper left) oxygen, magnesium, iron and alumimum. The red/yellow lines indicate the single count levels in 5 minutes for the five EHIS energy channels (per species). The heavy ion fluxes are ACE SIS verified L2 one-hour fluxes. ..... 27
Figure 7. The values of the dE/dL tables in LUT3 used to transform differential flux energy spectra into differential LET spectra. Note that the upper branches in the table are in fact negative; the values shown here are the absolute values as used in the transformation. Derived from SRIM stopping power output tables [Ziegler et al., 2008]. ..... 29
Figure 8. Event fluence spectra for the SEP event starting on 14 July 2000 (the Bastille Day event). The fluences are derived from the verified Level 2 1-hour SIS fluxes from the ACE Science Center. ..... 35
Figure 9. For the Bastille Day 2000 event, power law fits over the EHIS energy range (solid) and degraded spectra (dashed and dotted) after passing through 50 mil Al. The dashed (dotted) spectra correspond to degraded energies above (below) the energies of maximum electronic stopping power, indicated by the vertical lines. ..... 35
Figure 10. For the Bastille Day 2000 event, differential LET spectra, total (small diamonds) and by species. The solid (dotted) lines correspond to the upper (lower) branches. ..... 36
Figure 11. For the Bastille Day 2000 event, integral LET spectra, total (small diamonds) and by species. ..... 36
Figure 12. Event fluence spectra for the SEP event starting on 24 September 2001. The fluences are derived from the verified Level 2 1-hour SIS fluxes from the ACE Science Center. ..... 37

Figure 13. For the SEP event starting on 24 September 2001, power law fits over the EHIS energy range (solid) and degraded spectra (dashed and dotted) after passing through 50 mil Al. The dashed (dotted) spectra correspond to degraded energies above (below) the energies of maximum electronic stopping power, indicated by the vertical lines. ..... 37
Figure 14. For the SEP event starting on 24 September 2001, differential LET spectra, total (small diamonds) and by species. The solid (dotted) lines correspond to the upper (lower) branches. ..... 38
Figure 15. For the SEP event starting on 24 September 2001, integral LET spectra, total (small diamonds) and by species. ..... 38
Figure 16. Event fluence spectra for the SEP event starting on 15 April 2001. The fluences are derived from the verified Level 2 1-hour SIS fluxes from the ACE Science Center. ..... 39
Figure 17. For the SEP event starting on 15 April 2001, power law fits over the EHIS energy range (solid) and degraded spectra (dashed and dotted) after passing through 50 mil Al. The dashed (dotted) spectra correspond to degraded energies above (below) the energies of maximum electronic stopping power, indicated by the vertical lines. ..... 39
Figure 18. For the SEP event starting on 15 April 2001, differential LET spectra, total (small diamonds) and by species. The solid (dotted) lines correspond to the upper (lower) branches. ..... 40
Figure 19. For the SEP event starting on 15 April 2001, integral LET spectra, total (small diamonds) and by species. ..... 40
Figure 20. Differential and integral LET spectra in silicon for the Bastille Day 2000 event, under 50 mil Al shielding. ..... 41
Figure 21. Differential and integral LET spectra in silicon for the Bastille Day 2000 event, under 100 mil Al shielding. ..... 42
Figure 22. Differential and integral LET spectra in silicon for the Bastille Day 2000 event, under 500 mil Al shielding. ..... 43
Figure 23. Differential and integral LET spectra in silicon for the 15 April 2001 SEP event, under 100 mil Al shielding, assuming a 1-day accumulation period. All nine species are included. ..... 44
Figure 24. Differential and integral LET spectra in silicon for the 15 April 2001 SEP event, under 100 mil Al shielding, assuming a 1-hour accumulation period. Six species are included; N, Al and Si are omitted since the fluxes are too low to register above the single count level in at least 2 energy channels. ..... 45
Figure 25. Differential and integral LET spectra in silicon for the 15 April 2001 SEP event, under 100 mil Al shielding, assuming a 5-minute accumulation period. Only He is included; the other species are omitted since the fluxes are too low to register above the single count level in at least 2 energy channels. ..... 46

**LIST OF TABLES**

Table 1. Level 1b Heavy Ion Flux inputs to SEISS Solar Energetic Particle Event Linear Energy Transfer algorithm. ..... 18
Table 2. Maximum LET and associated energies for the nine projectile ion species used in the real-time LET algorithm. See Figure 2 for context. (Subscript B stands for the branch point.) ..... 29
Table 3. Level 2 Outputs of SEISS Solar Energetic Particle Event Linear Energy Transfer algorithm. ..... 31
Table 4. Selected shielding or moderator thicknesses in terms of areal density and equivalent thickness of aluminum. ..... 53

**LIST OF ACRONYMS**

| | |
|---|---|
| A | Atomic mass |
| ATBD | Algorithm Theoretical Basis Document |
| AWG | Algorithm Working Group |
| CIRES | Cooperative Institute for Research in Environmental Sciences |
| EHIS | Energetic Heavy Ion Sensor |
| eV | electron volt |
| FLUKA | FLUktuierende KAskade |
| FOV | field-of-view |
| JSC | Johnson Space Center (NASA) |
| keV | kilo-electron-volt |
| L1b | Level 1b |
| L2 | Level 2 |
| LET | linear energy transfer |
| MeV | mega-electron-volt |
| MeV/n or MeV/nuc | mega-electron volt per nucleon |
| MeV/u | mega-electron-volt per amu |
| NGDC | National Geophysical Data Center |
| pfu | particle flux unit |
| PORD | Performance and Operational Requirements Document |
| PRAL | Projected Range Algorithm |
| SEISS | Space Environment In-Situ Suite |
| SEP | solar energetic particle |
| SGPS | Solar and Galactic Proton Sensor |
| SPE | solar proton event |
| SRAG | Space Radiation Analysis Group |
| SRIM | Stopping and Range of Ions in Matter |
| SWPC | Space Weather Prediction Center |
| TRIM | Transport of Ions in Matter |
| Z | Atomic number |

**ABSTRACT**

The purpose of the L2+ Solar Energetic Particle Event Linear Energy Transfer algorithm is to transform energy spectra measured by the Energetic Heavy Ion Sensor (EHIS) into linear energy transfer (LET) spectra as a real-time indicator of potential radiation hazards for the satellite community. The charge deposited by a single high-LET particle can cause a single event effect (SEE) in electronics. The Workshop on Energetic Particle Measurements for the GOES-R+ Satellites (28-29 October 2002) articulated the satellite community's need for improved specification of the high-energy heavy-ion solar energetic particle (SEP) environment, expressed in units of LET (MeV $cm^2$/mg), which is more useful to the spacecraft design and testing communities than particle energy. The workshop report indicated that energy spectra of individual ion species measured by a spectrometer such as EHIS should be transformed into units of LET behind various thicknesses of spacecraft shielding. Adopting an idealized one-dimensional geometry, the L2+ SEP event LET algorithm estimates the LET spectrum in silicon behind selected spacecraft shielding thicknesses, after degrading the observed EHIS spectra due to transport through the shielding. The present version of this product is valid for unmanned spacecraft.

# 1.0 INTRODUCTION

## 1.1 Purpose of This Document

The purpose of this document is to describe the development and design of the SEISS algorithm for transforming EHIS heavy ion energy spectra into LET spectra, including details needed for implementation of the algorithm and examples of use and validation. It provides the operational requirements for this product and defines how these requirements are met with this algorithm. The algorithm inputs, processing and outputs are described in enough detail to design, develop, test and implement the necessary processing software and storage mechanisms.

## 1.2 Who Should Use This Document

The primary readership for this document includes those who have to implement the algorithm and those who seek to understand the algorithm as well as its assumptions and limitations. Members of the SWPC Space Weather Forecast Office should also use this ATBD to verify that their operational requirements are being met by the algorithm.

## 1.3 Inside Each Section

Section 2.0 OBSERVING SYSTEM OVERVIEW:
Describes the SEISS EHIS instrument and the measurements that serve as input to the algorithm.

Section 3.0 ALGORITHM DESCRIPTION:
Describes the development, theory and mathematics of the algorithm. Describes the logical flow of the algorithm, including input and output flow.

Section 4.0 TEST DATA SETS AND OUTPUTS:
Describes the test data sets used to characterize the performance of the algorithm and the data product quality. Describes the results from the algorithm processing on simulated input data.

Section 5.0 PRACTICAL CONSIDERATIONS:
Discusses issues involving numerical computation, programming and procedures, quality assessment and diagnostics and exception handling.

Section 6.0 ASSUMPTIONS AND LIMITATIONS:

Describes assumptions regarding input data contents and formats; instrument performance and characterization data; and potential future changes and improvements.

Section 7.0 REFERENCES:
Provides all references mentioned in the ATBD.

Appendix A REQUIREMENTS
Specifies the requirements for this algorithm.

Appendix B UNITS OF LET AND SHIELDING
Provides a reference for converting between different units of LET.

### 1.4 Related Documents

GOES-R Series Mission Requirements Document (MRD), P417-R-MRD-0070, Version 3.13, August 2, 2011.

Space Environment In-Situ Suite (SEISS) Performance and Operational Requirements Document (PORD), 417-R-SEISSPORD-0030, Baseline Version 2.9, November 12, 2010.

Ground Processing Algorithm Document for the GOES-R Space Environment In-Situ Suite (SEISS), SEISS-D-SY080, Rev. E, February 22, 2013.

### 1.5 Revision History

See p. 5.

# 2.0 OBSERVING SYSTEM OVERVIEW

## 2.1 Product Generated

Since the first GOES satellites, NOAA has used protons to characterize solar energetic particle (SEP) events. With the launch of GOES-R, NOAA is able to characterize SEP events in terms of heavy ions, which are of particular concern due to their large linear energy transfer (LET). For example, while helium ions have a maximum LET of 1.4 MeV $cm^2$ $mg^{-1}$ in silicon, iron ions have a maximum LET of 29.3 MeV $cm^2$ $mg^{-1}$ in silicon [Ziegler et al., 2008]. The charge deposited by a single high-LET particle can cause a single event effect (SEE) in an electronic part, both destructive (e.g., single-event latchup) and non-destructive (e.g., single-event transient).

The Workshop on Energetic Particle Measurements for the GOES-R+ Satellites (28-29 October 2002) articulated the satellite community's "…need for improved specification of the high-energy [>10 MeV/n] and high-Z [≥ 2] SEP environment, but expressed in units of LET (MeV/mg-$cm^2$) most useful to the spacecraft design and testing communities" [Mazur, 2002]. If a spectrometer were chosen to make the heavy ion measurement, then "…the energy spectra of individual ion species could be transformed into units of LET behind various thicknesses of spacecraft shielding for spacecraft engineering."

Because a spectrometer, the Energetic Heavy Ion Sensor (EHIS), was chosen to meet this requirement, we have developed just such an LET algorithm in order to make the EHIS measurements more immediately useful to the satellite community. Adopting an idealized one-dimensional geometry, we estimate what the LET spectrum would be in silicon behind selected spacecraft shielding thicknesses, after numerically degrading the observed EHIS spectra due to transport through the shielding. The purpose is to give the satellite community a real-time estimate of LET spectra so that they can judge the level of exposure of their LET-sensitive parts. They can then decide whether they should perform detailed three-dimensional modeling of the actual configuration. The present version of this product is valid for unmanned spacecraft, but it may be possible in the future to expand its range of validity to include typical shielding levels in manned spacecraft.

Although it is part of the Event Detection product, the LET product is produced by a separate module from the main Event Detection product, from EHIS rather than SGPS fluxes Because of this independence, the LET algorithm has its own ATBD. This separation improves the clarity of both the LET and the Event Detection ATBDs.

## 2.2 Instrument Characteristics

The SEISS operational requirements and characteristics are detailed in section 3.3.6.1 of the GOES-R Series Mission Requirements Document (MRD, P417-R-MRD-0070) and the SEISS Performance and Operational Requirements Document (PORD, 417-R-SEISSPORD-0030). The requirements pertaining specifically to energetic heavy ions, which are pertinent to the linear energy transfer (LET) algorithm, are in section 3.3.6.1.1 of the MRD and 3.2.4 of the PORD.

SEISS is a suite of five particle sensors: magnetospheric particle sensors in a low-energy and high-energy range (MPS-LO and -HI), two solar and galactic proton sensors (SGPS), and an energetic heavy ion sensor (EHIS). The EHIS is based on the Angle Detecting Inclined Sensor (ADIS) system [Connell et al., 2001, 2007]. EHIS measures heavy ion fluxes in five energy channels above 10 MeV/n, separating the elements from hydrogen through nickel. These energies are significantly relativistic, as determined by the Lorentz factor $\gamma$:

$$\gamma = 1 + \frac{E_c}{A_1 m_p c^2} \tag{1}$$

where $E_c$ is the channel center energy in MeV, $A_1$ is the atomic mass of the ion, and $m_p c^2$ is the proton rest mass (938 MeV). The Lorentz factor is plotted in Figure 1 for the lowest and highest energy channels, E1 and E5, as a function of atomic number ($Z_1$).

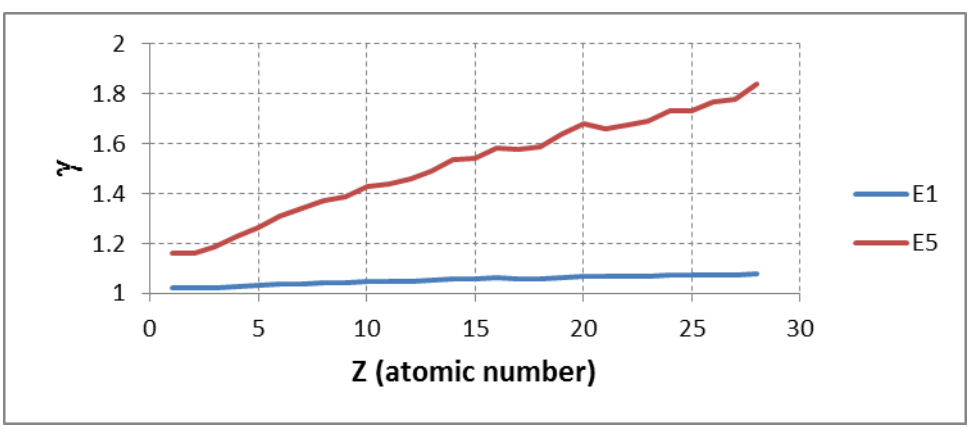


**Figure 1. Lorentz factor γ for EHIS channels E1 and E5 as a function of the heavy ion atomic number. (CDR estimates.)**

# 3.0 ALGORITHM DESCRIPTION

## 3.1 Algorithm Overview

The LET algorithm calculates 0.1 - 30 MeV $cm^2$ $mg^{-1}$ total (summed over species) linear energy transfer (LET) differential [$cm^{-2}$ $s^{-1}$ $sr^{-1}$ (MeV $cm^2$ $mg^{-1}$)$^{-1}$] and integral [$cm^{-2}$ $s^{-1}$ $sr^{-1}$] spectra from EHIS heavy ion flux energy spectra. It calculates LET in Silicon behind 50, 100, and 500 mils of Aluminum in a one-dimensional geometry.

It is instructive to consider the government's 0.1-100 MeV $cm^2$ $mg^{-1}$ LET requirement in the NPOESS IORD II (December 10, 2001). Of the elements that are likely to be observed above the EHIS noise floor in a 5-minute interval, iron (Fe) has the greatest peak LET in silicon, 29.3 MeV $cm^2$ $mg^{-1}$. Of ions heavier than Fe, EHIS measures cobalt and nickel; nickel (with a peak LET in silicon of 31.4 MeV $cm^2$ $mg^{-1}$) will be observed in event fluences. Over the EHIS energy range, only helium (He) and carbon (C) have LETs below 0.1 MeV $cm^2$ $mg^{-1}$. So while integral LET spectra and total (i.e., summed over species) differential LET spectra can be provided above 0.1 MeV $cm^2$ $mg^{-1}$, most of the elements will not have differential LET spectra down to 0.1 MeV $cm^2$ $mg^{-1}$.

## 3.2 Processing Outline

1. Fit a power law to EHIS L1b heavy ion energy spectra with at least two fluxes greater than an upper limit.
2. Using pre-calculated look-up tables, simulate the transport of these spectra though selected thicknesses of aluminum shielding.
3. Using pre-calculated tables of stopping power, transform the transported energy spectra into differential LET spectra and sum them over species.
4. Calculate integral LET spectra and sum them over species.

## 3.3 Algorithm Input

The inputs to the algorithm consist of EHIS L1b fluxes on a 5-min cadence.

### 3.3.1 Primary Data

The input L1b heavy ion flux quantities are defined in Table 1.

**Table 1. Level 1b Heavy Ion Flux inputs to SEISS Solar Energetic Particle Event Linear Energy Transfer algorithm.**

| Data Type | Refresh | Number of values | Units |
|---|---|---|---|
| Helium differential fluxes for 5 energy intervals | 5 min | 5 | particles / ($cm^2$ s sr (MeV/n)) |
| Helium energy boundaries, upper and lower, for 5 energy intervals | 5 min | 5 x 2 | MeV/n |
| Statistical uncertainties in Helium differential fluxes for 5 energy intervals | 5 min | 5 | particles / ($cm^2$ s sr (MeV/n)) |
| Heavy ion (Be-Cu) differential fluxes for 5 energy intervals | 5 min | 5 x 26 | particles / ($cm^2$ s sr (MeV/n)) |
| Heavy ion (Be-Cu) energy boundaries, upper and lower, for 5 energy intervals | 5 min | 5 x 26 x 2 | MeV/n |
| Statistical uncertainties (upper and lower) in Heavy ion (Be-Cu) differential fluxes for 5 energy intervals | 5 min | 5 x 26 x 2 | particles / ($cm^2$ s sr (MeV/n)) |
| Time | 5 min | 2 (start and end times of accumulation period) | Seconds since J2000 epoch. |

### 3.3.2 Ancillary Data

No ancillary data are required by the algorithm.

## 3.4 Theoretical Description

The LET algorithm has two primary components: (1) transport of the heavy ion spectra through aluminum shelding, and (2) transformation of the resulting degraded flux spectra from energy to LET in silicon. The physics of the two are closely related.

### 3.4.1 Physics of the Problem

Mass stopping power $S/\rho = dE/(\rho dl)$ is the mean energy lost by charged particles in traversing a path length $dl$ in a target of mass density $\rho$ (typically with units of MeV $cm^2$ $mg^{-1}$), while linear stopping power is simply $S = dE/dl$ (typically with units of keV/μm) [Sigmund, 2004; ICRU, 2011]. Linear stopping power has three additive components, electronic ($S_{el}$), radiative ($S_{rad}$), and nuclear ($S_{nuc}$). As distinct from stopping power,

linear energy transfer (LET) is defined [ICRU, 2011, section 4.5] as the linear electronic stopping power minus the mean sum of kinetic energies greater than some energy Δ of electrons released by the ion as it traverses the target over length *dl*. This energy cutoff Δ indicates energy carried away by energetic secondary electrons such that it is not deposited locally. If Δ is set to infinity, then the LET is known as the *unrestricted* linear energy transfer and is equal to $S_{el}$. The LET ($L$) calculated by this algorithm is in fact the mass electronic stopping power (MeV $cm^2$ $mg^{-1}$). While both electronic and nuclear stopping power are included in the modeled transport through aluminum, only electronic stopping power in silicon is used to transform the transported energy spectra to LET spectra.

Charged projectile particles lose energy during their transport through the target through seven processes [Sigmund, 2004, pp. 20-21]: (1) excitation and ionization of target electrons (a.k.a. electronic stopping), (2) excitation and ionization of the projectile, (3) electron capture, (4) recoil loss (a.k.a. nuclear stopping), (5) electromagnetic radiation, (6) nuclear reactions, and (7) chemical reactions. The first five contribute to stopping, and electronic stopping is the dominant stopping process in our energy range.

The present version of the GOES-R SEP LET algorithm is based on the Stopping and Range of Ions in Matter (SRIM) model, including the Transport of Ions in Matter (TRIM) Monte-Carlo code and the Projected Range Algorithm (PRAL) for calculating stopping and range tables [Ziegler et al., 2008]. SRIM accounts for energy loss processes (1) through (4) above. SRIM determines the stopping and range of ions using theory that is in good agreement with an extensive collection of accurate experimental data. Projectile ions lose energy separately to the nuclei and the electrons in the material; nuclear stopping is only important at the lowest energies. For the relativistic energies (> 10 MeV/n) measured by EHIS (Figure 1), SRIM uses relativistic Bethe-Bloch electronic stopping theory, with energy-dependent corrections [Ziegler et al., 2008, p. 4-35]. The degree to which the charge of the projectile is affected by passage through the target is important in calculating stopping; SRIM accounts for both electron capture at low energies and electron loss at high energies. SRIM also includes the effects of straggling, or the distribution of energy loss about the mean.

SRIM is rich in theoretical depth and has been validated extensively through comparison with data (see for example the website of Dr. Helmut Paul at the University of Linz, http://www.exphys.uni-linz.ac.at/Stopping/). Paul and Schinner [2005] and Paul [2006] show that, in the EHIS energy range (>10 MeV/n), electronic stopping power tables from SRIM-2003 agree with experimental stopping power data to within 1% for H and He and within 5% for Li to Ar in several solids. SRIM96 was shown to be in good agreement with CREME96, some minor discrepancies not significantly affecting calculation of single event effects [Tylka et al., 1997]. (SRIM-2008 is used in the present work.) Therefore, in terms of electronic and nuclear stopping, SRIM provides an accurate basis for calculating LET (Figure 2).

Electromagnetic radiation (bremsstrahlung) is an important energy loss process for relativistic electrons passing through typical spacecraft and instrument shielding [Cayton and Tuszewski, 2005], but for heavy ions it is a dominant process, along with electron-positron pair production, only above $10^6$ MeV/n [Sørensen, 2003; Sigmund, 2004, p. 34]. Chemical reactions are not significant at keV and greater energies [Sigmund, 2004, p. 21]: Therefore, the only projectile energy loss process not included in SRIM that can be significant in space radiation applications is nuclear reactions, which cause a change in the mass or identity of the projectile. For example, the creation of secondaries via nuclear fragmentation is included in CREME 96 [Tylka et al., 1997].

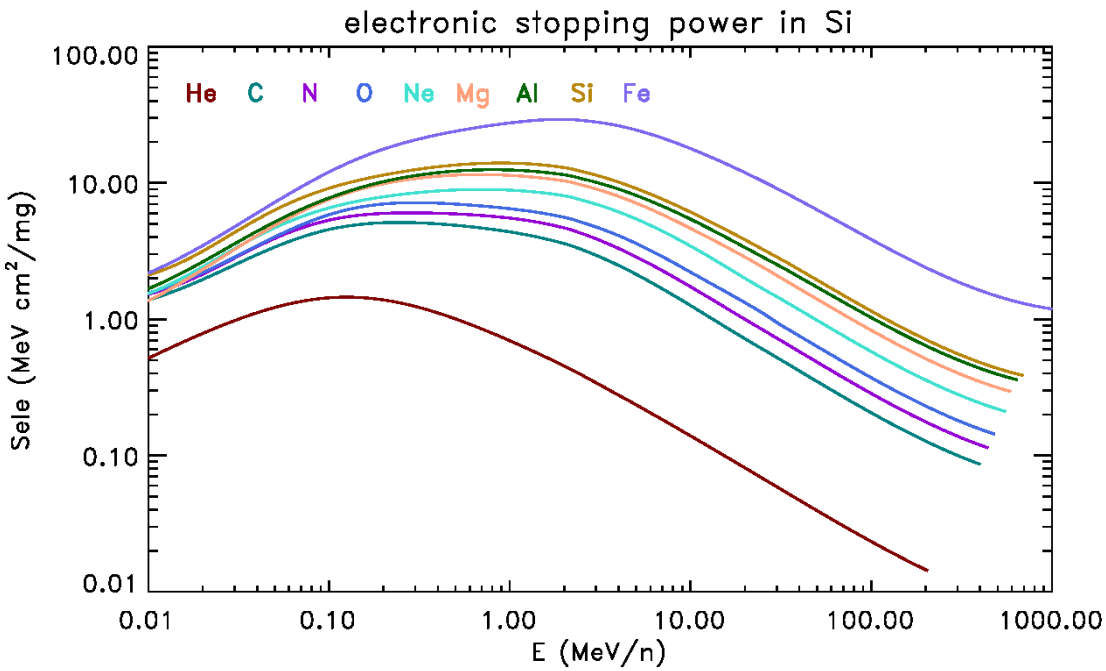


**Figure 2. Electronic mass stopping power (Sele/ρ) in silicon of the most abundant heavy ions in solar energetic particle events, below the maximum EHIS energy (by species). From SRIM PRAL [Ziegler et al., 2008].**

The omission of nuclear fragmentation in the present version of the GOES-R SEP LET algorithm is justified by the small shielding thicknesses of aluminum chosen for the algorithm. The effects of fragmentation are first noticeable at $l = 10$ g cm$^{-2}$ or 1457 mil Al [Adams, 1983], while the largest thickness in the present version is 500 mil. However, nuclear reaction cross-sections increase with increasing projectile energy and with increasing ratio of path length to range, as well as with decreasing atomic mass of both the projectile and the target [Geissel et al., 2002]. (This is why beryllium targets are used to produce lower mass fragments from primary beams [Sigmund, 2004, p. 95], as in the EHIS calibration experiments.) For example, at the center of the highest EHIS energy channel for Ne ($A_1 = 20$), ~400 MeV/n or ~8 GeV, the range $R$ of Ne in Al is 78.67 mm

[Ziegler et al., 2008]. The ratio of path length to range for 500 mil or 12.7 mm shielding is $l/R$ = 12.7/78.67 = 0.16. Geissel et al. [2002] show that for $l/R$ = 0.1, the nuclear reaction probability for a 400 MeV/n Ne ion is ~7%, which is significant though not dominant. However, at these relativistic energies, where the Ne fluxes are little degraded after transport through the Al shielding, their LET in Si (0.24 MeV $cm^2$ $mg^{-1}$) is about 2.7% of the maximum (8.95 MeV $cm^2$ $mg^{-1}$). This suggests that the effect of neglecting nuclear reactions on the LET spectra is indeed small for 500 mil (3.4 g $cm^{-2}$) or thinner shielding. However, nuclear reactions (fragmentation) are important for predicting the effect of heavy ions through shielding appropriate to manned spacecraft (of order 10 g $cm^{-2}$) [Zeitlin et al., 2008]. Therefore, if the validity range of this algorithm is extended to manned spacecraft, nuclear fragmentation will have to be accounted for. This will require using another model instead of TRIM to generate the transport look-up tables. See the section below on "Pre-Planned Product Improvements."

According to the CREME website, "Most proton-induced single-event effects (SEEs) are due to nuclear recoils from target atoms rather than direct ionization. Inclusion of protons in LET spectra can lead to gross overestimates in SEE rate. Proton-induced SEE cross sections are characterized vs. proton energy." Therefore, we do not include the observed proton spectra in this LET calculation. The 5-minute proton flux energy spectra should be sufficient for use by the community. Nuclear stopping of protons is also an important component of non-ionizing energy loss (NIEL) below 50 MeV [Jun et al., 2003]. NIEL results in displacement damage which is a cause of long-term degradation of semiconductor devices or optical detectors in the space environment. This algorithm does not address NIEL or SEEs due to protons.

### 3.4.2 Mathematical Description

*Definition of Quantities*

| | |
|---|---|
| $A_1$ | mass number of projectile ion (atomic mass units, amu) |
| $Z_1$ | atomic number of projectile ion |
| $A_2$ | mass number of target atom (atomic mass units, amu) |
| $Z_2$ | atomic number of target atom |
| S | stopping power (MeV/μm) |
| $S_{ele}$ | electronic stopping power (MeV/μm) |
| $S/\rho$ | mass stopping power (MeV $cm^2$ $mg^{-1}$) |
| L | LET = $S_{ele}/\rho$ (MeV $cm^2$ $mg^{-1}$) |
| $L_B(Z_1,Z_2)$ | maximum LET of projectile (Z1) in target (Z2); B refers to the branch point |

| | |
|---|---|
| d | thickness of aluminum shielding |
| $j_i(E_i,Z_1)$ | differential ion flux of atomic number $Z_1$ vs. energy, incident on shielding ($cm^{-2}$ $s^{-1}$ $sr^{-1}$ $(MeV/n)^{-1}$) |
| $j_d(E_d,Z_1,d)$ | differential ion flux of atomic number $Z_1$ vs energy, degraded in energy and flux by transport through aluminum shielding of thickness d ($cm^{-2}$ $s^{-1}$ $sr^{-1}$ $(MeV/n)^{-1}$) |
| $j(L,Z_1,Z_2,d)$ | differential ion flux of atomic number $Z_1$ vs. LET in target material of atomic number $Z_2$ after transport through aluminum shielding of thickness d ($cm^{-2}$ $s^{-1}$ $sr^{-1}$ $(MeV\ cm^2/mg)^{-1}$) |
| $j(L,Z_2,d)$ | total differential ion flux vs. LET in target material of atomic number $Z_2$ after transport through aluminum shielding of thickness d ($cm^{-2}$ $s^{-1}$ $sr^{-1}$ $(MeV\ cm^2/mg)^{-1}$) |
| $J(>L,Z_1,Z_2,d)$ | integral ion flux of atomic number $Z_1$ vs. LET in target material of atomic number $Z_2$ after transport through aluminum shielding of thickness d ($cm^{-2}$ $s^{-1}$ $sr^{-1}$) |
| $J(>L,Z_2,d)$ | total integral ion flux vs. LET in target material of atomic number $Z_2$ after transport through aluminum shielding of thickness d ($cm^{-2}$ $s^{-1}$ $sr^{-1}$) |

The particle kinetic energies are defined in terms of energy per nucleon, which is approximately the same (within 0.25% for stable isotopes of Li and heavier elements) as kinetic energy per amu ($E/A_1$).

*Definition of Coarse and Fine Interpolation Grids*

The energy grid on which the SRIM-output stopping power tables are defined is species-dependent, as is the energy grid of the look-up tables generated using TRIM. The latter dependence is driven by the species-dependent range in aluminum, requiring finer sampling (and more Monte-Carlo runs) around the energies that have non-unity probability of passing through a given thickness of shielding. However, the LET spectra for the different species need to be on the same grid when they are summed to give total spectra. Therefore, a common LET interpolation grid is defined, consisting of a coarse grid and a fine grid. The coarse grid consists of of 101 logarithmically-spaced LETs between 0.1 and 30 MeV $cm^2$ $mg^{-1}$. This coarse grid in LET avoids all of the maximum LETs by species, so that the singularities at the maximum LETs can be handled by a Taylor series expansion (see below). The fine grid consists of nine islands of 9 linearly spaced points between (but not including) the maximum LETs by species (Table 2) and the nearest lower coarse grid point.

*Power Law Fit to EHIS L1b Fluxes*

The EHIS L1b fluxes are fit to a power law using a linear fit of $\log_{10}$(flux) vs. $\log_{10}$(center energy). Define the power law as

$$j_i(E_i, Z_i) = j_0 E_i^{-\gamma} \tag{2}$$

Then

$$\log_{10} j_i\,(E_i, Z_i) = \log_{10} j_0 - \gamma \log_{10} E_i \tag{3}$$

The center energy is determined as the geometric mean of the energy band edges reported in real-time in the L1b records. It is likely (Figure 6) that fewer than five valid points will be present for a given species at five minute intervals. This is determined by evaluating the upper and lower statistical uncertainties provided in the L1b records (Table 1). According to CDRL080 Rev E, section 6.2.5, for ions heavier than helium, if the lower statistical uncertainty is equal to the histogram fit value (the reported flux), then only an upper limit exists (mean plus one-sigma), and the reported flux should not be used in the power-law fit. If only one valid spectral point is available, the fit cannot be performed and the species is not included in the LET calculation.

*Transport through Shielding*

The first look-up table, calculated using a transport code like TRIM, is a multiplicative factor that degrades the incident ion energy to the energy of the ions emerging from the shielding:

$$LUT1 = T_1(E_i; E_d, Z_1, d) \tag{4}$$

$$E_d = T_1(E_i; E_d, Z_1, d) E_i \tag{5}$$

The second look-up table, calculated from the same transport results as LUT1, degrades the incident ion flux due to transport through aluminum shielding of thickness d:

$$LUT2 = T_2(j_i; j_d, Z_1, d) \tag{6}$$

$$j_d(E_d, Z_1, d) = T_2(j_i; j_d, Z_1, d) j_i(E_i, Z_1) \tag{7}$$

Examples of LUT1 and LUT2 are shown in Figure 3. They are finely sampled around the ion energy at which the ion range in aluminum is the same as the thickness of the aluminum shielding, and more coarsely at higher energies.

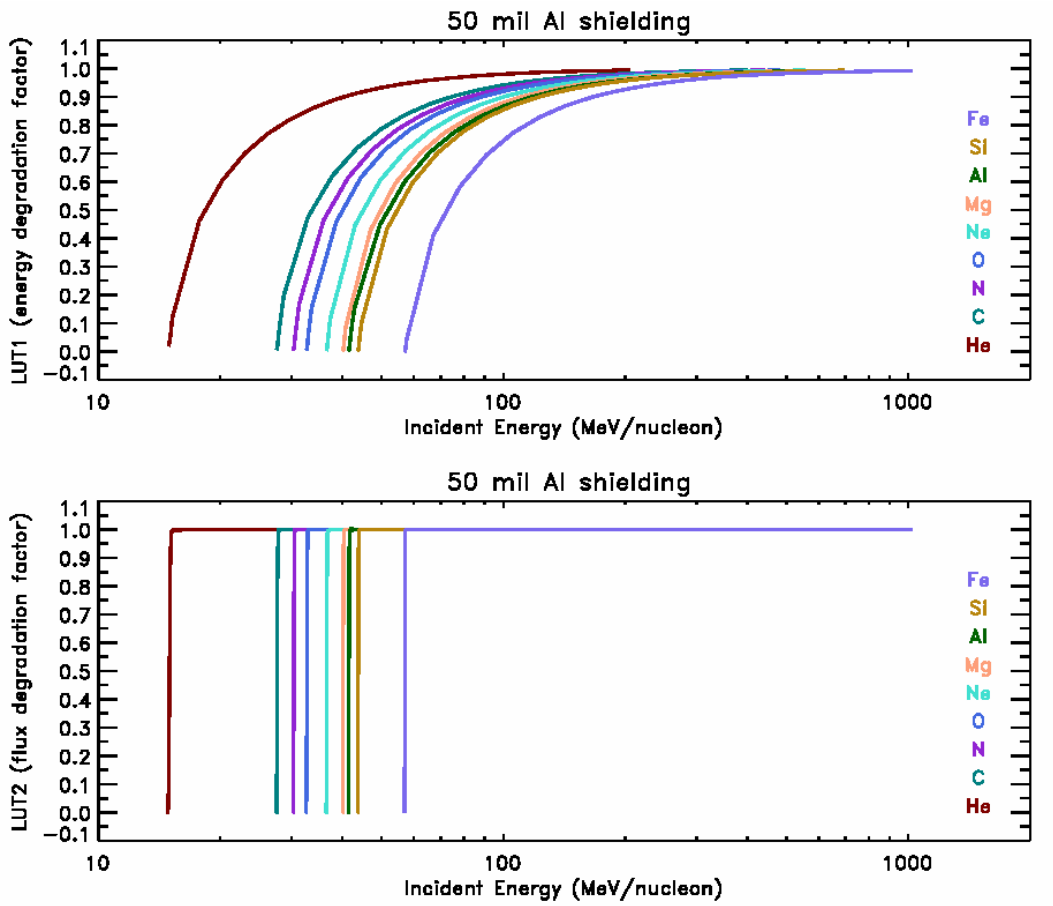


**Figure 3. Look-up tables LUT1 (energy degradation) and LUT2 (flux degradation) for energies appropriate to 50 mil aluminum shielding and the nine projectile species included in the real-time LET algorithm.**

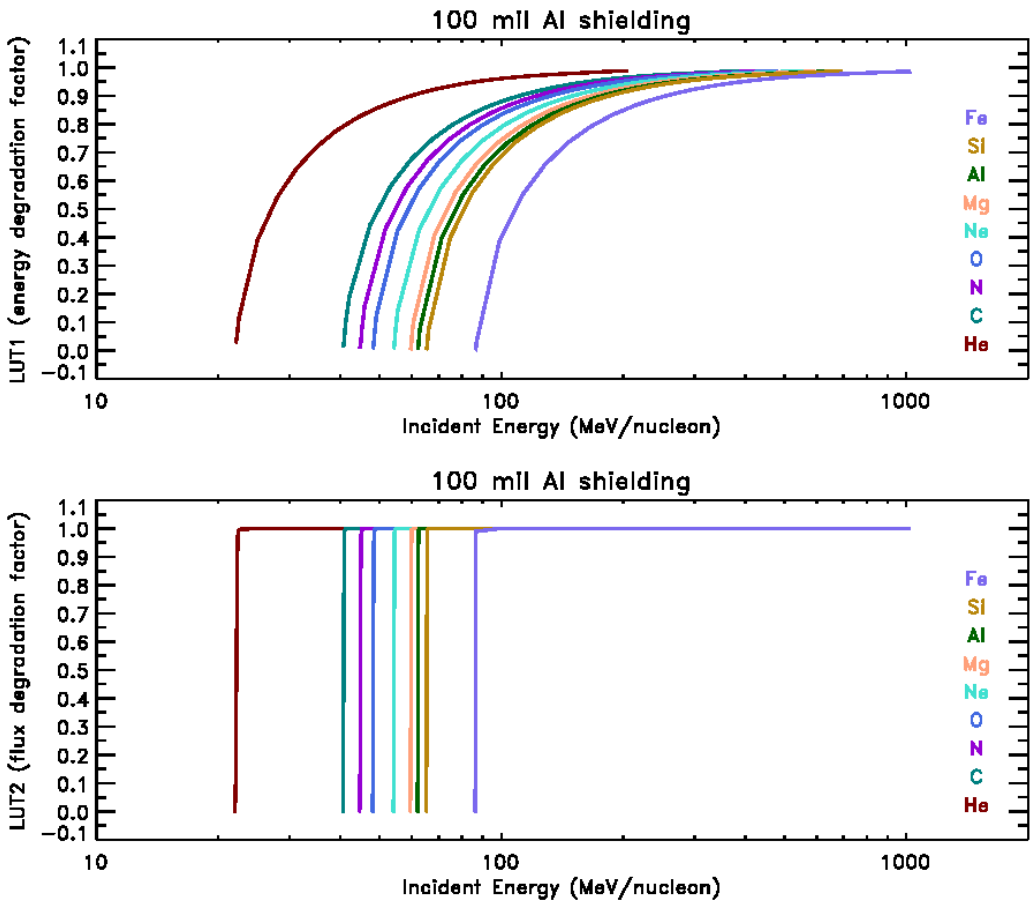


**Figure 4. Look-up tables LUT1 (energy degradation) and LUT2 (flux degradation) for energies appropriate to 100 mil aluminum shielding and the nine projectile species included in the real-time LET algorithm.**

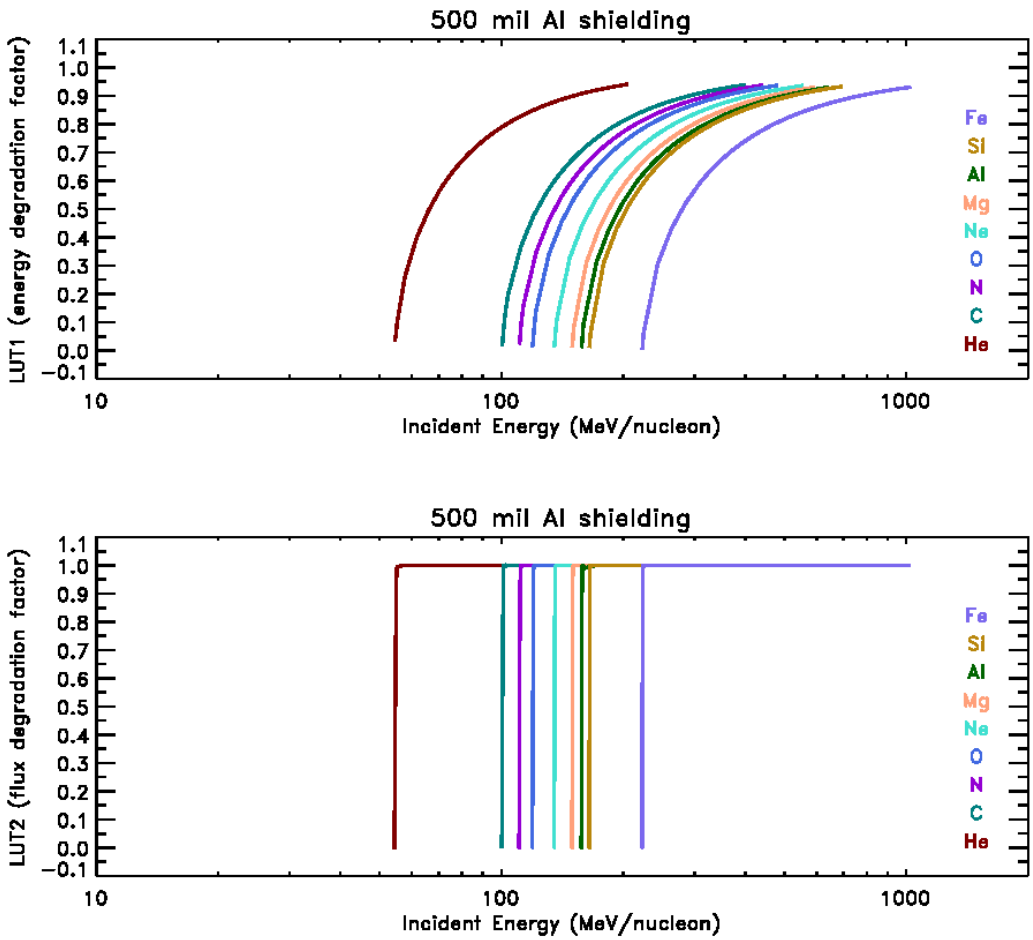


**Figure 5. Look-up tables LUT1 (energy degradation) and LUT2 (flux degradation) for energies appropriate to 500 mil aluminum shielding and the nine projectile species included in the real-time LET algorithm.**

Although EHIS separately measures the ion fluxes for 25 elements between beryllium and nickel, in addition to helium and hydrogen, only a small fraction of these will be observed above the noise floor in the real-time 5-minute-averaged fluxes. Therefore, the real-time algorithm has LUTs only for a subset of these elements. We determined the elements for which to construct tables by comparing the peak fluxes in the 22 largest SEP events from Solar Cycle 23 (SC23) to the single count level in EHIS (calculated using CDR-maturity geometrical factor and energy bands for a 5-minute accumulation period). The heavy ion fluxes were Level 2 verified 1-hour average fluxes measured by the Solar Isotope Spectrometer (SIS) [Stone et al., 1998] on the Advanced Composition Explorer (ACE). These 1-hour fluxes are produced for the 14 most abundant species (apart from hydrogen). Of these, we found that nine elements had peak fluxes above the single count level at least once in SC23 (He, C, N, O, Ne, Mg, Al, Si and Fe). Plots of the peak

spectra from SC23 events are shown in Figure 6 for four elements. Based on these results, the real-time L2+ algorithm will have LUTs for these nine elements. Of these nine, Al is the most marginal. The LUTs used in the real-time analysis are reported as a quality indicator.

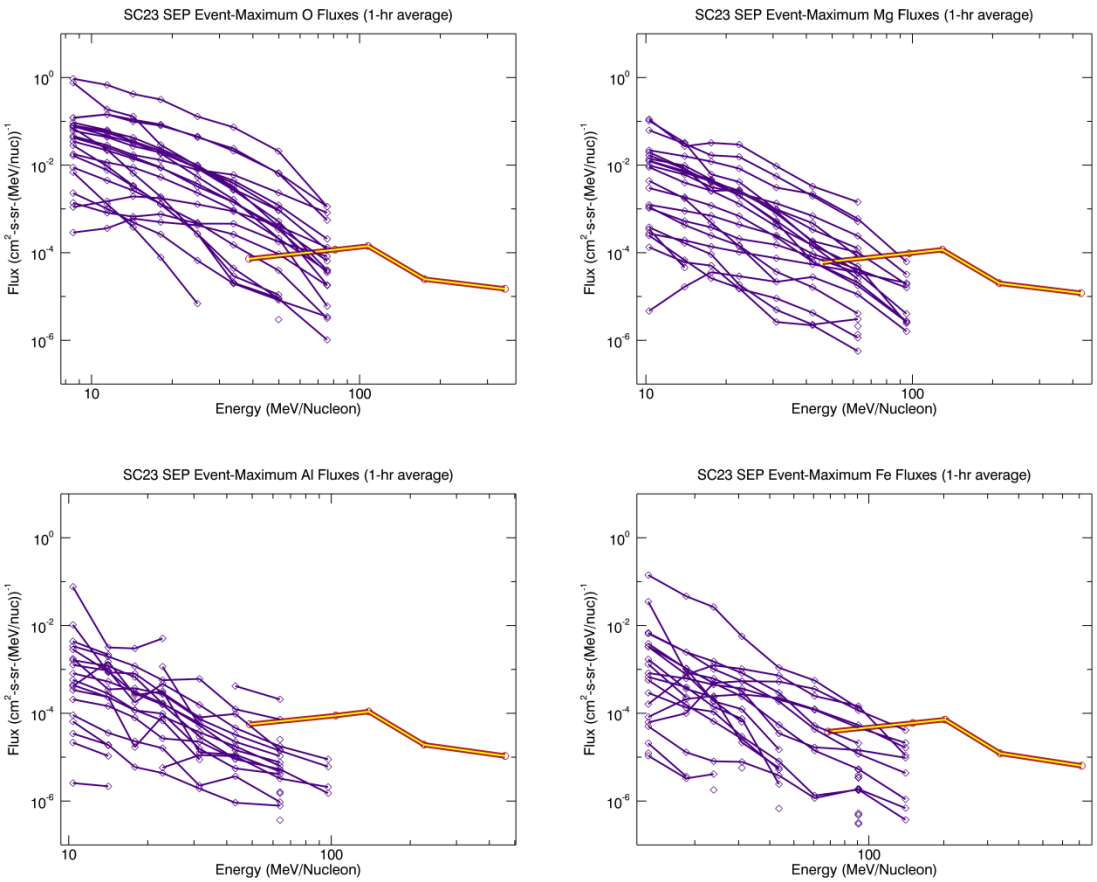


**Figure 6. Maximum flux spectra for the 22 largest SEP events in Solar Cycle 23 for (clockwise from upper left) oxygen, magnesium, iron and alumimum. The red/yellow lines indicate the single count levels in 5 minutes for the five EHIS energy channels (per species). The heavy ion fluxes are ACE SIS verified L2 one-hour fluxes.**

*Transformation from Energy to LET*

The energy-to-LET transformation component of the LET algorithm is based on the work of Heinrich [1977], with an important refinement by Badavi et al. [2005].

The degraded flux spectrum, $j_d(E_d,Z_1,d)$, is differential in kinetic energy. Therefore, conceptually it is simple to transform it to being differential in LET:

$$j(L, Z_1, Z_2, d) = j_d(E_d, Z_1, d) \left|\frac{dE}{dL}\right| \tag{8}$$

However, there are several complications that make this a non-trivial algorithm to implement. First, the relationship between E and L is not monotonic (Figure 2). Therefore, dE/dL has multiple branches. Over the EHIS energy range, it has two branches. The upper branch is negative; therefore, the absolute value of the derivative must be used in the transformation. Second, as these two branches approach maximum L, dE/dL goes to infinity. (This results in the peaks observed in differential LET spectra.) Therefore, there are multiple singularities (one per ion species) to be handled. Third, calculating derivatives from tabulated values needs to be done properly or the results will be noisy. Finally, the validity range of the result is limited by the energy range of the EHIS measurements, which varies by ion species. Therefore, the algorithm must avoid extrapolation to unobserved parameter space or the results could be invalid.

The LUT that is used to transform the energy spectrum to an LET spectrum is defined as:

$$LUT3 = \frac{dE}{dL}\,(E_d, Z_1, Z_2, b) \tag{9}$$

where b indicates the upper or lower branch. LUT3 also includes the coarse and fine LET grids defined above. First, the SRIM PRAL stopping power tables are interpolated to the coarse LET grid defined above, treating L as the independent variable and E as the dependent variable. They are separated into lower (energy) and upper (energy) branches. Extrapolation outside the valid range of the tables (by species) is strictly avoided.

The first derivatives dE/dL are calculated at the table points k as

$$E'_k = \frac{E_{k+1} - E_k}{L_{k+1} - L_k} - \frac{1}{3}(L_{k+1} - L_k)\left(E''_k + \frac{1}{2}E''_{k+1}\right) \tag{10}$$

$$E'_{k+1} = \frac{E_{k+1} - E_k}{L_{k+1} - L_k} + \frac{1}{3}(L_{k+1} - L_k)\left(\frac{1}{2}E''_k + E''_{k+1}\right) \tag{11}$$

where the second derivatives at the table points are calculated as one would for initializing a natural cubic spline interpolation [Press et al., 1988, pp. 94-96]. One of these equations can be used except at an edge, where the other is needed. Since the coarse LET grid avoids all of the species-maximum LETs, this derivative is never infinite for LUT3. (To be clear, LUT3 is precalculated, not during run-time.) The contents of LUT3 for the nine species used in the real-time calculation are plotted in Figure 7.

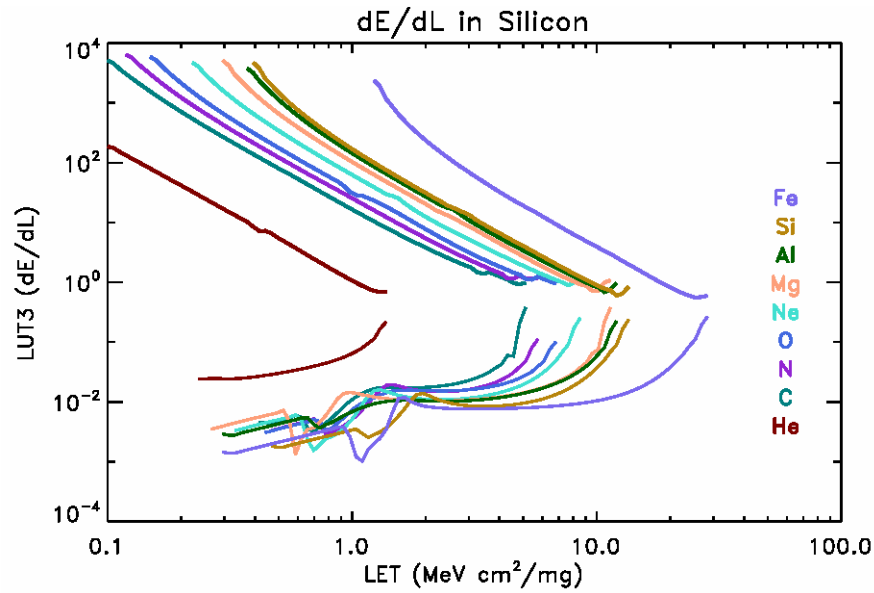


**Figure 7. The values of the dE/dL tables in LUT3 used to transform differential flux energy spectra into differential LET spectra. Note that the upper branches in the table are in fact negative; the values shown here are the absolute values as used in the transformation. Derived from SRIM stopping power output tables [Ziegler et al., 2008].**

Once LUT3 is used to estimate the LET flux for each branch on the coarse interpolation grid, the problem remains of estimating the flux for LETs close to the maximum LETs. A regular interpolation grid cannot be expected to properly sample LET space near the maximum LETs for each of the nine ion species (Table 2). In order to deal with this problem, we adapt the Taylor series expansion approach developed by Badavi et al. [2005] in order to estimate the flux on a fine grid just below each of the maximum LETs. The result is an expression for the LET flux near the branch point that is a function of LET and the flux at the nearest coarse interpolation point.

**Table 2. Maximum LET and associated energies for the nine projectile ion species used in the real-time LET algorithm. See Figure 2 for context. (Subscript B stands for the branch point.)**

| | He | C | N | O | Ne | Mg | Al | Si | Fe |
|---|---|---|---|---|---|---|---|---|---|
| $L_B$ (MeV cm$^2$ mg$^{-1}$). | 1.45 | 5.13 | 6.04 | 7.17 | 8.95 | 11.5 | 12.5 | 14.0 | 29.3 |
| $E_B$ (MeV/n) | 0.13 | 0.24 | 0.28 | 0.30 | 0.71 | 0.70 | 0.82 | 0.89 | 2.0 |

At the peak of the LET vs. energy curves (Figure 2), the first derivative dL/dE is zero. Therefore, the Taylor series expansion for LET near the peak (the branch point B) is given by:

$$L(E) \cong L(E_B) + \frac{(E - E_B)^2}{2} L''(E_B) \tag{12}$$

and the first derivative near the branch point is given by

$$\frac{dL}{dE} \cong (E - E_B)L''(E_B) \tag{13}$$

These two expressions can be combined to give

$$\frac{dL}{dE} \cong \sqrt{2|L(E) - L_{\boldsymbol{B}}||L''(E_B)|} \tag{14}$$

Given that

$$j(L) = j(E)/|dL/dE| \tag{15}$$

if we assume that j(E) varies little over this narrow LET range, we can relate the flux at the nearest coarse interpolation point Li to the flux at the desired LET as

$$j(L) \cong j(L_i)\sqrt{\frac{|L_i - L_B|}{|L - L_B|}} \tag{16}$$

where $L_i < L < L_B$ [Badavi et al., 2005]. Therefore, j(L) increases as L approaches the branch point, as expected for the LET peak. In the current version of the algorithm, the interval between $L_i$ and $L_B$ is divided linearly into a fine grid of ten equal segments, so this Taylor series method is used to extrapolate $j(L_i)$ to nine points L between $L_i$ and $L_B$.

The flux is estimated on this fine grid for all of the ion species, not just the one approaching its maximum LET, so that they may be summed more easily. However, for the other species, linear interpolation in linear flux vs. linear LET is used rather than a Taylor series expansion. The end result of this section is differential flux vs. LET for each species on the common coarse and fine grids. The coarse and fine grids, and the corresponding LET spectra, are concatenated and sorted from lowest to highest LET (0.1 to 30 MeV $cm^2$/mg).

*Differential LET Flux Determination*

The differential LET flux for each species is determined by summing the fluxes on the lower and higher energy branches:

$$j(L, Z_1, Z_2, d) = j_{upper}(L, Z_1, Z_2, d) + j_{lower}(L, Z_1, Z_2, d) \tag{17}$$

The upper-energy-branch flux is dominant, except near the branch point, where the lower branch also makes a significant contribution to the total.

Next, the differential LET flux is summed over projectile species $Z_1$ to give the total differential LET spectrum:

$$j(L, Z_2, d) = \sum_{Z_1} j(L, Z_1, Z_2, d) \tag{18}$$

Recall that the differential LET fluxes are already determined on a common LET grid.

*Integral LET Flux Determination*

The integral flux (by species) is determined from the differential flux using the trapezoidal rule. Each interpolation point successively serves as the lower limit to the integral.

$$J(> L, Z_1, Z_2, d) = \frac{1}{2} \sum_{i=i(L)}^{i_{max}-1} [j(L_{i+1}) + j(L_i)] \, (L_{i+1} - L_i) \tag{19}$$

where i(L) is the index corresponding to L and $i_{max}$ is the total number of interpolation points (coarse + fine). The interval $L_{i+1}$-$L_i$ varies due to the logarithmic spacing of the coarse interpolation grid and the admixture of the fine grids.

Finally, the total (summed over projectile species) integral LET flux is calculated from the total differential flux as

$$J(> L, Z_2, d) = \frac{1}{2} \sum_{i=i(L)}^{i_{max}-1} [j(L_{i+1}, Z_2, d) + j(L_i, Z_2, d)] \, (L_{i+1} - L_i) \tag{20}$$

### 3.4.3 Algorithm Output

The outputs of the real-time LET algorithm are summarized in Table 3.

**Table 3. Level 2 Outputs of SEISS Solar Energetic Particle Event Linear Energy Transfer algorithm.**

| **Data Type** | **Refresh** | **Number of values** | **Units** |
|---|---|---|---|
| Time | 5 min | 2 (start and end times of accumulation period) | Seconds since J2000 epoch. |
| Input spectrum validity flags, He | 5 min | 5 | Unitless (one flag per energy channel, 1 = valid, 0 = not valid) |
| Input spectrum validity flags, C, N, O, Ne, Mg, Al, Si, Fe | 5 min | 5 x 8 | Unitless (one flag per energy channel, 1 = valid, 0 = not valid) |

| **Data Type** | **Refresh** | **Number of values** | **Units** |
|---|---|---|---|
| LET output grid | 5 min | 182 | MeV $cm^2$ $mg^{-1}$ |
| Differential LET spectrum for He, 50-mil Al | 5 min | 182 | particles / ($cm^2$ s sr (MeV $cm^2$ $mg^{-1}$)) |
| Differential LET spectra for C, N, O, Ne, Mg, Al, Si, Fe, 50-mil Al | 5 min | 8 x 182 | particles / ($cm^2$ s sr (MeV $cm^2$ $mg^{-1}$)) |
| Total differential LET spectrum, 50-mil Al | 5 min | 182 | particles / ($cm^2$ s sr (MeV $cm^2$ $mg^{-1}$)) |
| Integral LET spectrum for He, 50-mil Al | 5 min | 182 | particles / ($cm^2$ s sr) |
| Integral LET spectra for C, N, O, Ne, Mg, Al, Si, Fe, 50-mil Al | 5 min | 8 x 182 | particles / ($cm^2$ s sr) |
| Total integral LET spectrum, 50-mil Al | 5 min | 182 | particles / ($cm^2$ s sr) |
| Differential LET spectrum for He, 100-mil Al | 5 min | 182 | particles / ($cm^2$ s sr (MeV $cm^2$ $mg^{-1}$)) |
| Differential LET spectra for C, N, O, Ne, Mg, Al, Si, Fe, 100-mil Al | 5 min | 8 x 182 | particles / ($cm^2$ s sr (MeV $cm^2$ $mg^{-1}$)) |
| Total differential LET spectrum, 100-mil Al | 5 min | 182 | particles / ($cm^2$ s sr (MeV $cm^2$ $mg^{-1}$)) |
| Integral LET spectrum for He, 100-mil Al | 5 min | 182 | particles / ($cm^2$ s sr) |
| Integral LET spectra for C, N, O, Ne, Mg, Al, Si, Fe, 100-mil Al | 5 min | 8 x 182 | particles / ($cm^2$ s sr) |
| Total integral LET spectrum, 100-mil Al | 5 min | 182 | particles / ($cm^2$ s sr) |
| Differential LET spectrum for He, 500-mil Al | 5 min | 182 | particles / ($cm^2$ s sr (MeV $cm^2$ $mg^{-1}$)) |
| Differential LET spectra for C, N, O, Ne, Mg, Al, Si, Fe, 500-mil Al | 5 min | 8 x 182 | particles / ($cm^2$ s sr (MeV $cm^2$ $mg^{-1}$)) |
| Total differential LET spectrum, 500-mil Al | 5 min | 182 | particles / ($cm^2$ s sr (MeV $cm^2$ $mg^{-1}$)) |
| Integral LET spectrum for He, 500-mil Al | 5 min | 182 | particles / ($cm^2$ s sr) |

| **Data Type** | **Refresh** | **Number of values** | **Units** |
|---|---|---|---|
| Integral LET spectra for C, N, O, Ne, Mg, Al, Si, Fe, 500-mil Al | 5 min | 8 x 182 | particles / ($cm^2$ s sr) |
| Total integral LET spectrum, 500-mil Al | 5 min | 182 | particles / ($cm^2$ s sr) |

# 4.0 TEST DATA SETS AND OUTPUTS

## 4.1 Simulated/Proxy Input Data Sets

The method used here for developing a proxy data set for EHIS is described in detail by Bharath et al. [2013]. In brief, the proxy data are developed from measurements by the Solar Isotope Spectrometer (SIS) aboard the Advanced Composition Explorer (ACE) satellite [Stone et al., 1998]. ACE is located at the L1 Lagrangian point; the heavy ion fluxes measured by GOES-R are expected to be similar to those observed at L1, particularly at higher energies. The SIS Level 2 product available from the ACE Science Center includes hourly-averaged fluxes of the fourteen most abundant elements from helium to nickel in eight energy bands that vary by element but lie in the range from 4 to 150 MeV/n. The upper four SIS energy bands overlap the lower part of the EHIS energy range. Therefore, the measured SIS spectra are extrapolated to the higher energy EHIS channels as described by Bharath et al. [2013]. We scale the event fluence spectra generated by Bharath et al. [2013] to the peak oxygen flux observed in SIS channel 7 (49.8 MeV/n) during a given SEP event, in order to illustrate the magnitude of LET in real-time near the peak of an event. The case in which some of the spectral fluxes are below background levels is simulated by estimating the counts using the as-delivered EHIS geometrical factors and band energies and using a different accumulation time (e.g., 300 s, 3600 s, 86,400 s) for each proxy data file. If the calculated counts are less than one, the flux and statistical errors (both the upper and lower error, in the case of the Be-Cu ions) are set to the single count level ($1 = jG\Delta E\Delta t$). In the EHIS L1b CDRL80, the condition of equality of the flux and the lower statistical error indicates that the reported flux is an upper bound to the actual flux, resulting from the non-linear multi-Gaussian fit.

## 4.2 Test Results Using Proxy Input Data

For three SEP events from Solar Cycle 23, we show (1) event fluence spectra, (2) incident and degraded differential flux energy spectra behind 50 mil aluminum shielding, (3) differential LET flux spectra (both branches and sum), and (4) integral LET flux spectra. The three events are the Bastille Day 2000 event (Figure 8 through Figure 11); the 24 September 2001 event, with a relatively low iron abundance (Figure 12 through Figure 14); and the 15 April 2001 event, with a relatively high iron abundance (Figure 17 through Figure 19). In general, the upper energy branches of the differential spectra dominate, except approaching the branch point for the higher LET species, where it is important to include the lower branch in the flux estimation. The spikes at the species-maximum LETs are characteristic of differential LET spectra [Heinrich, 1977].

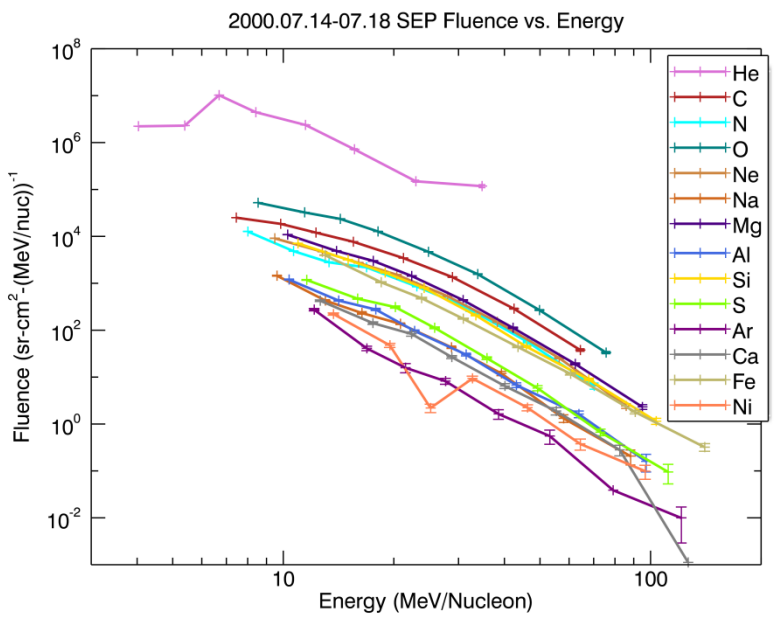


**Figure 8. Event fluence spectra for the SEP event starting on 14 July 2000 (the Bastille Day event). The fluences are derived from the verified Level 2 1-hour SIS fluxes from the ACE Science Center.**

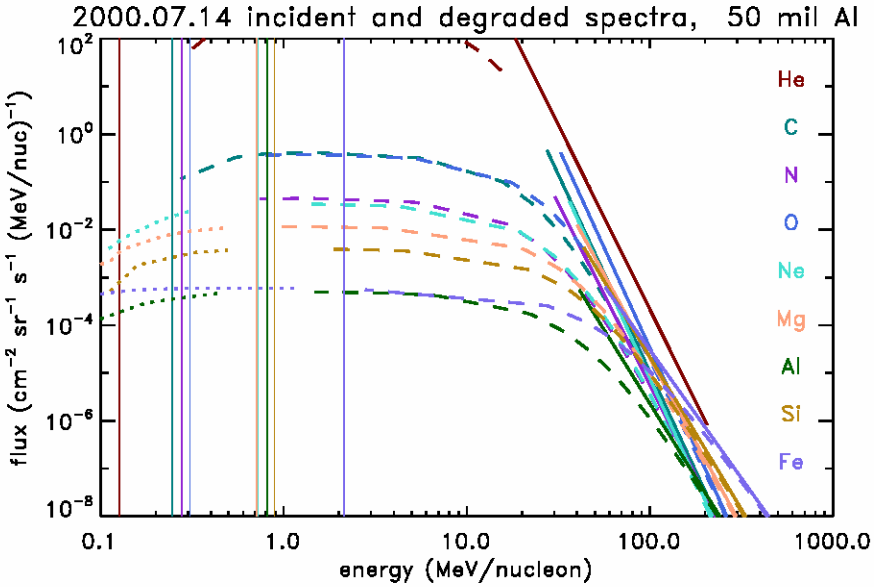


**Figure 9. For the Bastille Day 2000 event, power law fits over the EHIS energy range (solid) and degraded spectra (dashed and dotted) after passing through 50 mil Al. The dashed (dotted) spectra correspond to degraded energies above (below) the energies of maximum electronic stopping power, indicated by the vertical lines.**

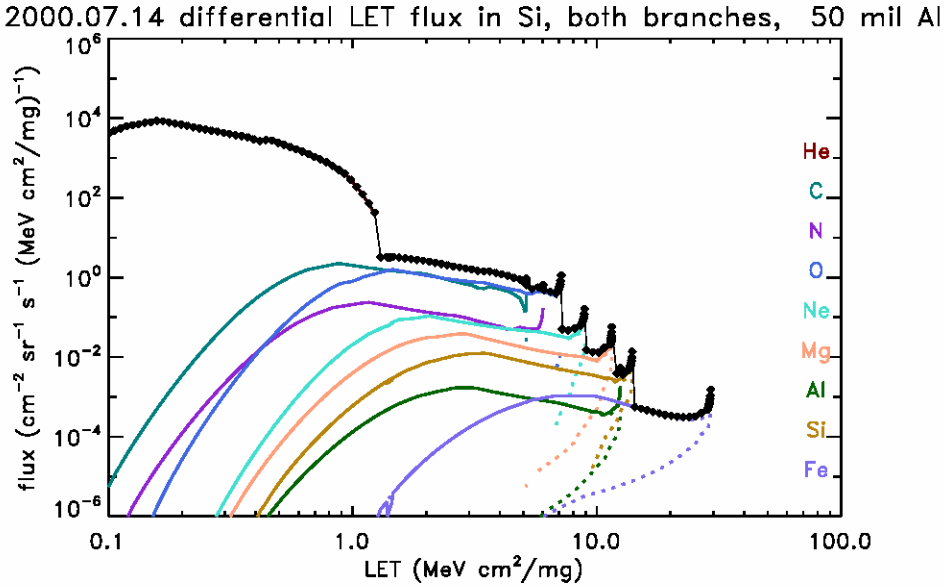


**Figure 10. For the Bastille Day 2000 event, differential LET spectra, total (small diamonds) and by species. The solid (dotted) lines correspond to the upper (lower) branches.**

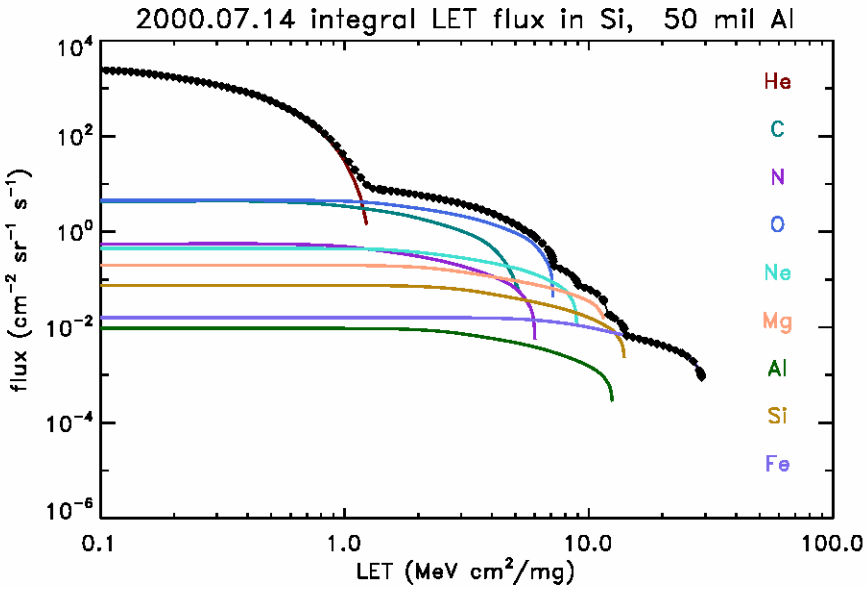


**Figure 11. For the Bastille Day 2000 event, integral LET spectra, total (small diamonds) and by species.**

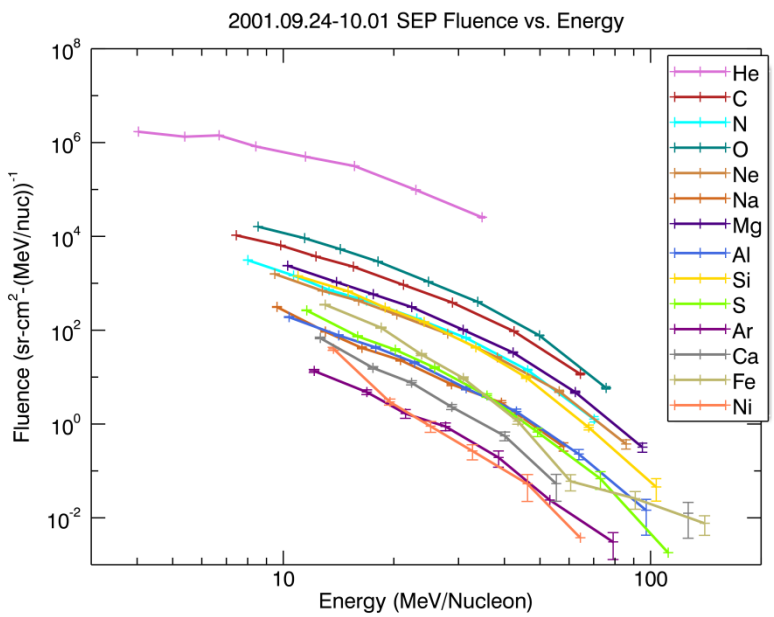


**Figure 12. Event fluence spectra for the SEP event starting on 24 September 2001. The fluences are derived from the verified Level 2 1-hour SIS fluxes from the ACE Science Center.**

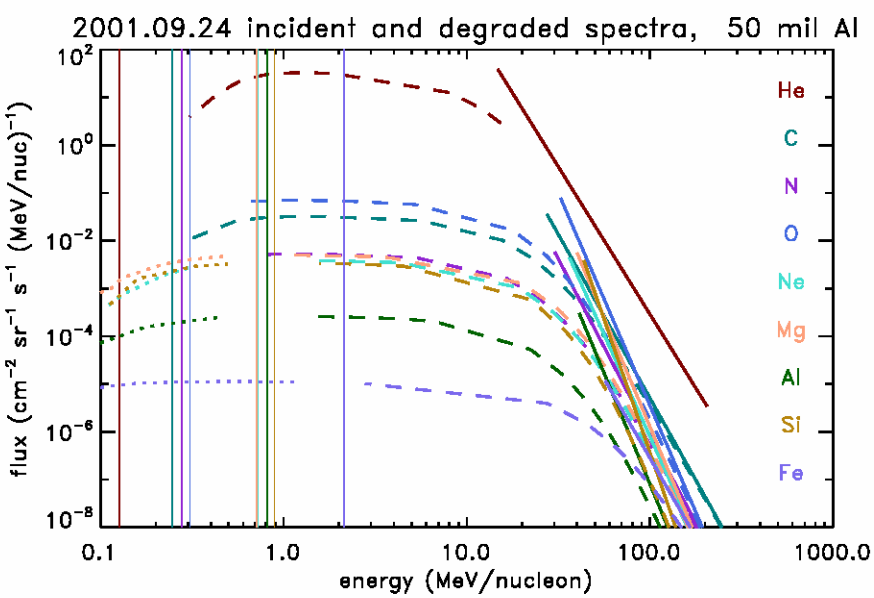


**Figure 13. For the SEP event starting on 24 September 2001, power law fits over the EHIS energy range (solid) and degraded spectra (dashed and dotted) after passing through 50 mil Al. The dashed (dotted) spectra correspond to degraded energies above (below) the energies of maximum electronic stopping power, indicated by the vertical lines.**

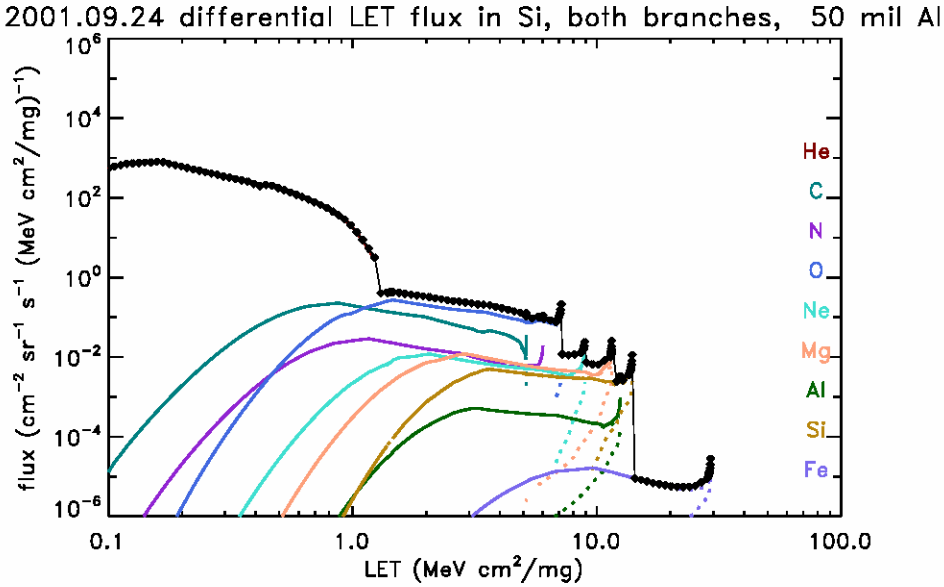


**Figure 14. For the SEP event starting on 24 September 2001, differential LET spectra, total (small diamonds) and by species. The solid (dotted) lines correspond to the upper (lower) branches.**

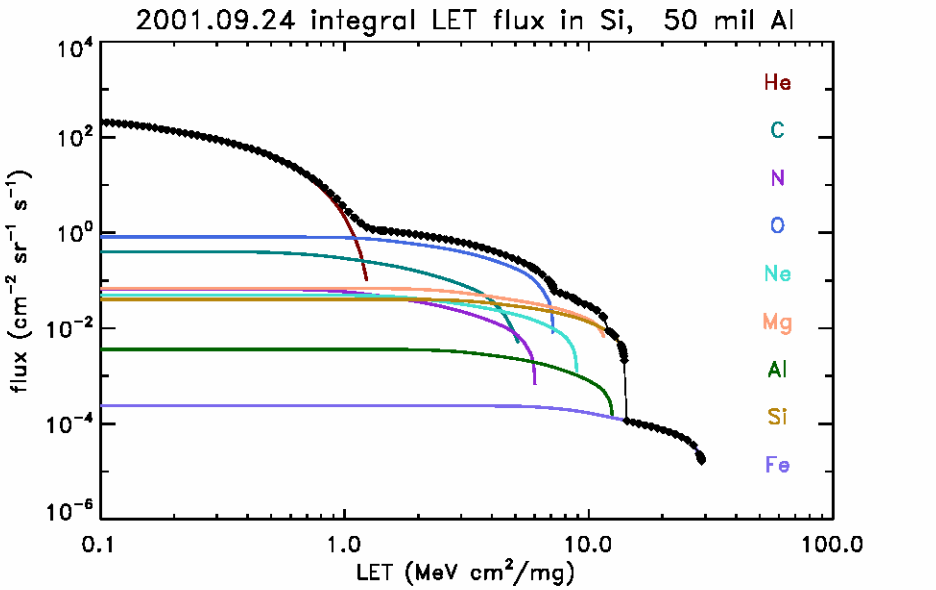


**Figure 15. For the SEP event starting on 24 September 2001, integral LET spectra, total (small diamonds) and by species.**

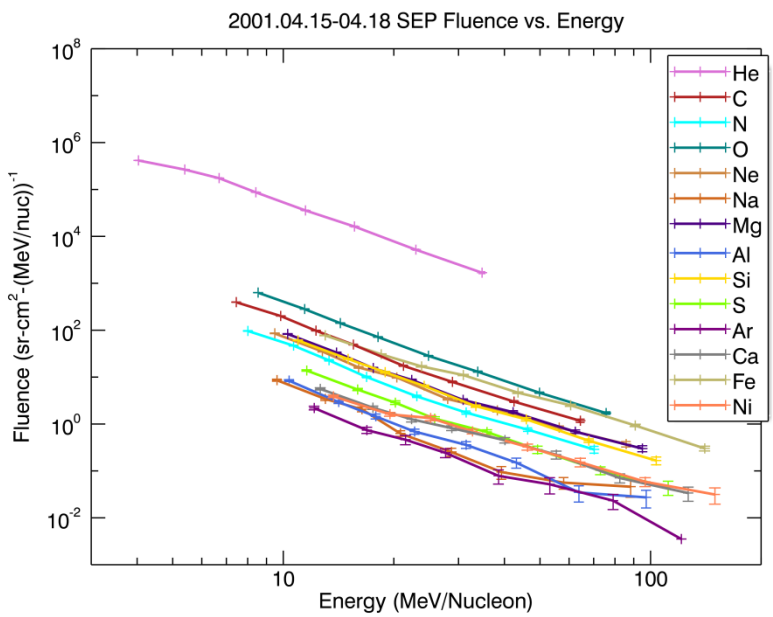


**Figure 16. Event fluence spectra for the SEP event starting on 15 April 2001. The fluences are derived from the verified Level 2 1-hour SIS fluxes from the ACE Science Center.**

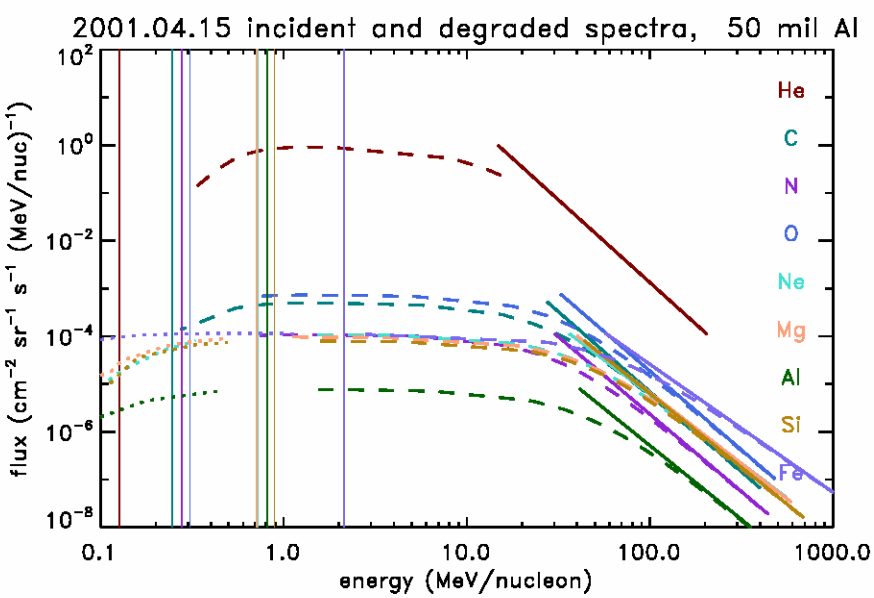


**Figure 17. For the SEP event starting on 15 April 2001, power law fits over the EHIS energy range (solid) and degraded spectra (dashed and dotted) after passing through 50 mil Al. The dashed (dotted) spectra correspond to degraded energies above (below) the energies of maximum electronic stopping power, indicated by the vertical lines.**

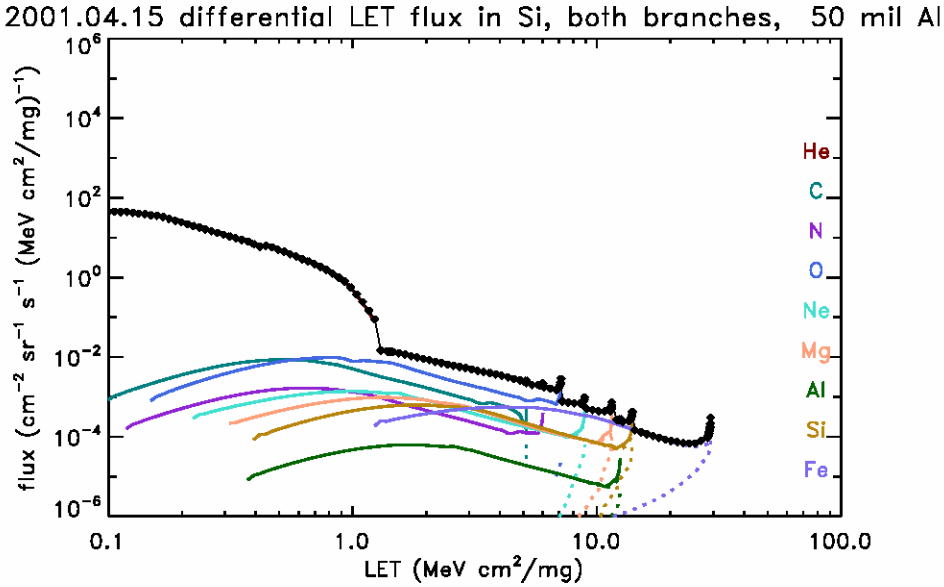


**Figure 18. For the SEP event starting on 15 April 2001, differential LET spectra, total (small diamonds) and by species. The solid (dotted) lines correspond to the upper (lower) branches.**

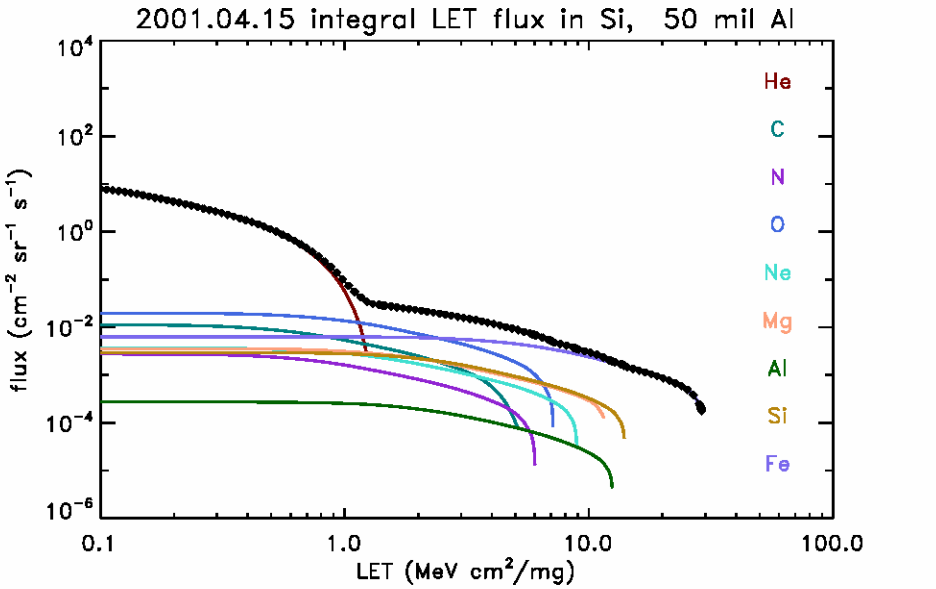


**Figure 19. For the SEP event starting on 15 April 2001, integral LET spectra, total (small diamonds) and by species.**

Figure 20, Figure 21 and Figure 22 illustrate the effects of different thicknesses of aluminum shielding, using the Bastille Day 2000 event as an example. Figure 23, Figure 24, and Figure 25 illustrate the effects of decreasing accumulation time and resulting omission of certain species from the LET calculation, using the 15 April 2001 event and 100-mil aluminum shielding as an example.

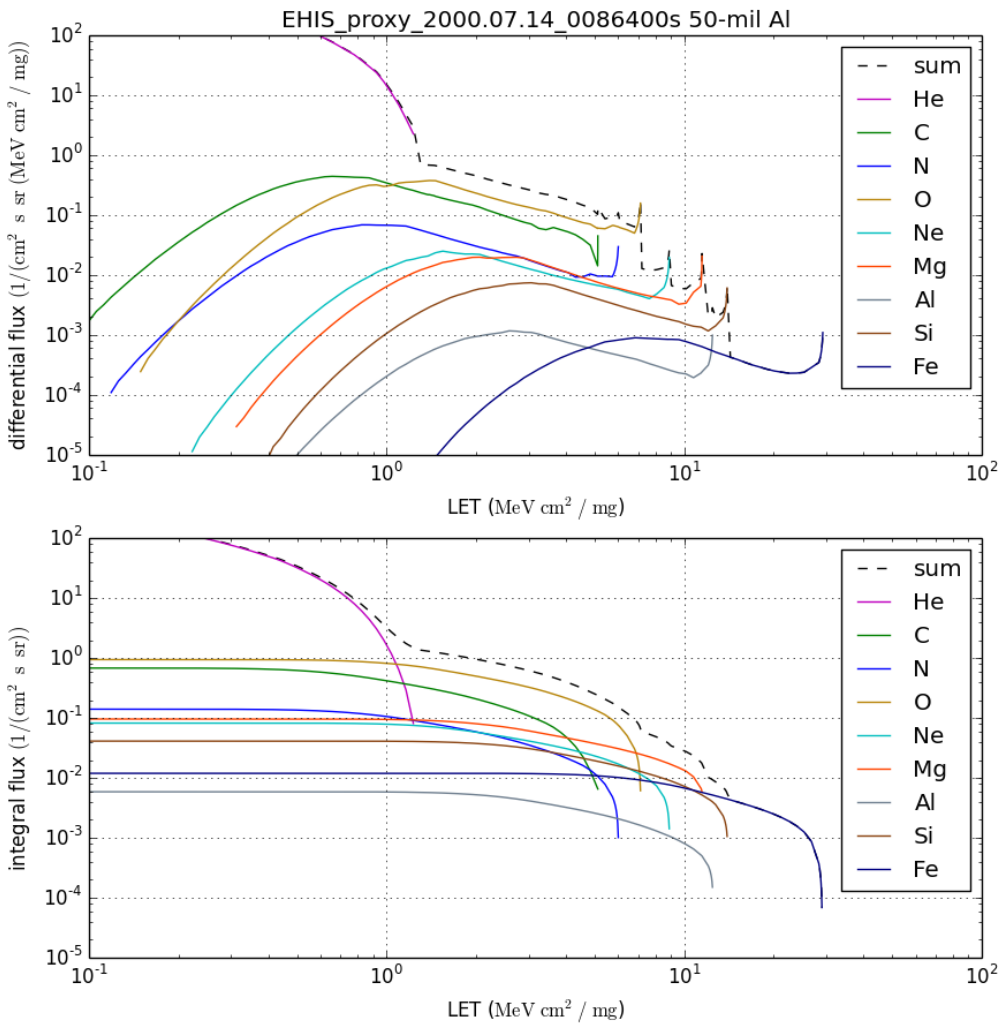


**Figure 20. Differential and integral LET spectra in silicon for the Bastille Day 2000 event, under 50 mil Al shielding.**

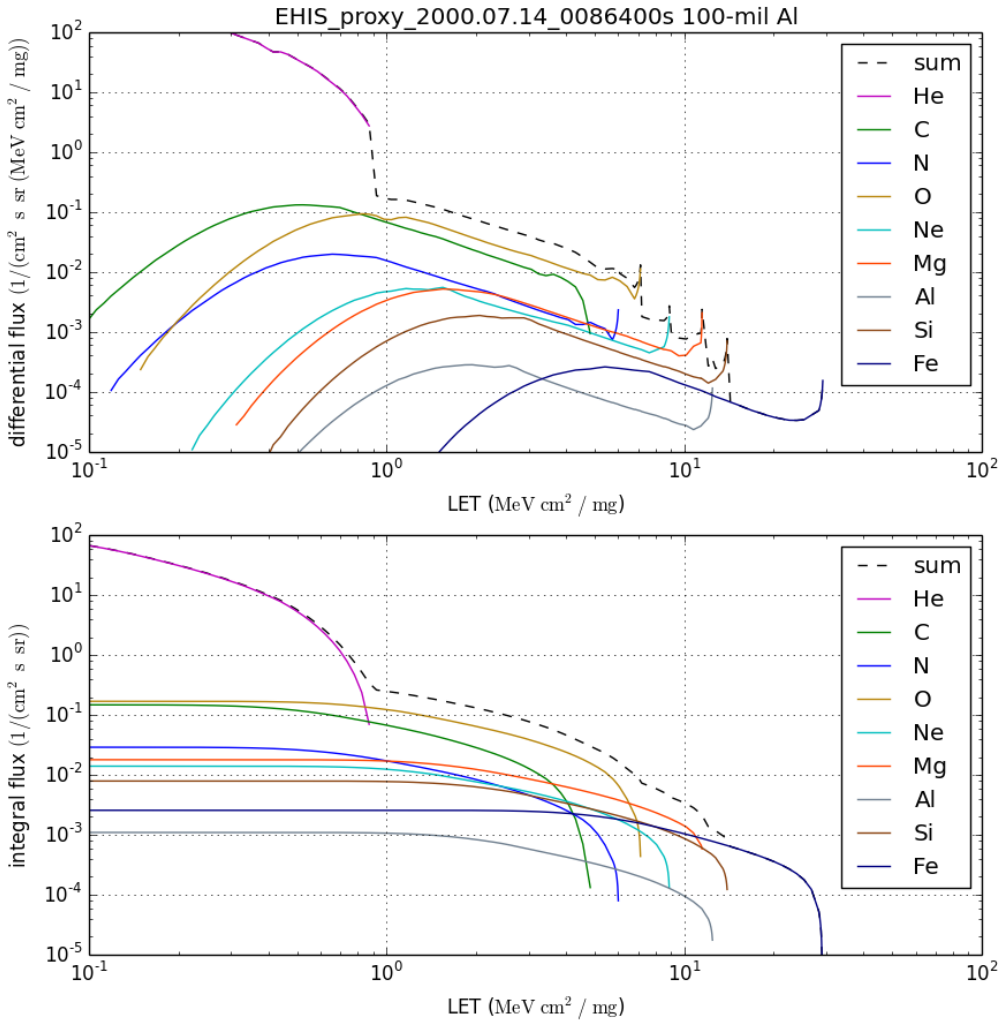


**Figure 21. Differential and integral LET spectra in silicon for the Bastille Day 2000 event, under 100 mil Al shielding.**

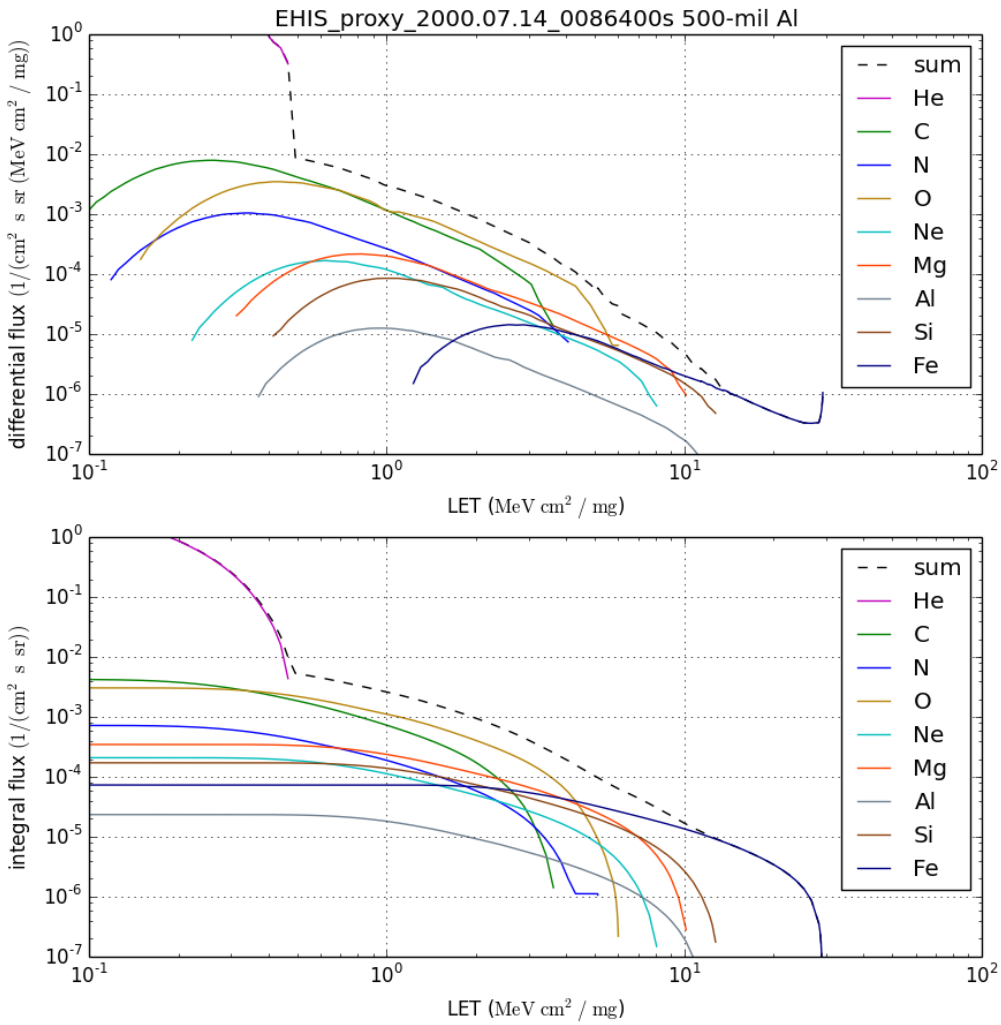


**Figure 22. Differential and integral LET spectra in silicon for the Bastille Day 2000 event, under 500 mil Al shielding.**

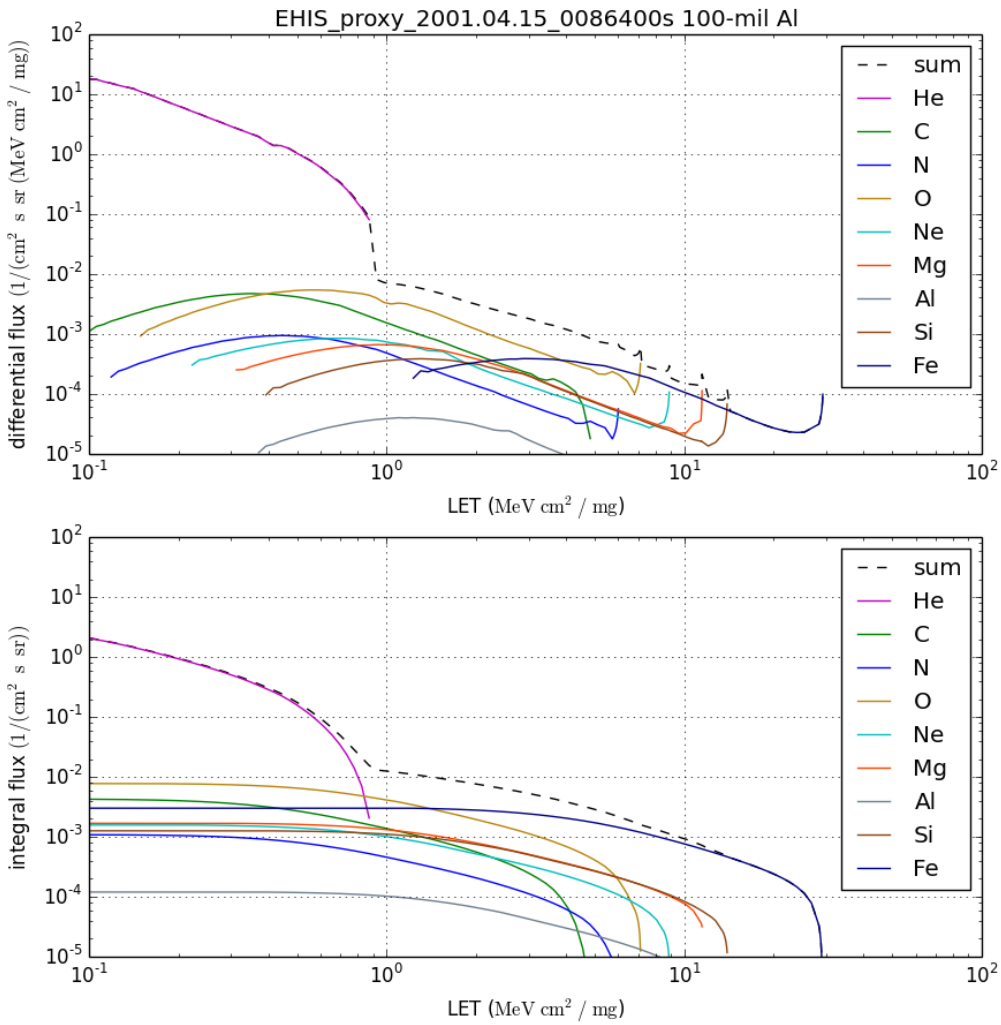


**Figure 23. Differential and integral LET spectra in silicon for the 15 April 2001 SEP event, under 100 mil Al shielding, assuming a 1-day accumulation period. All nine species are included.**

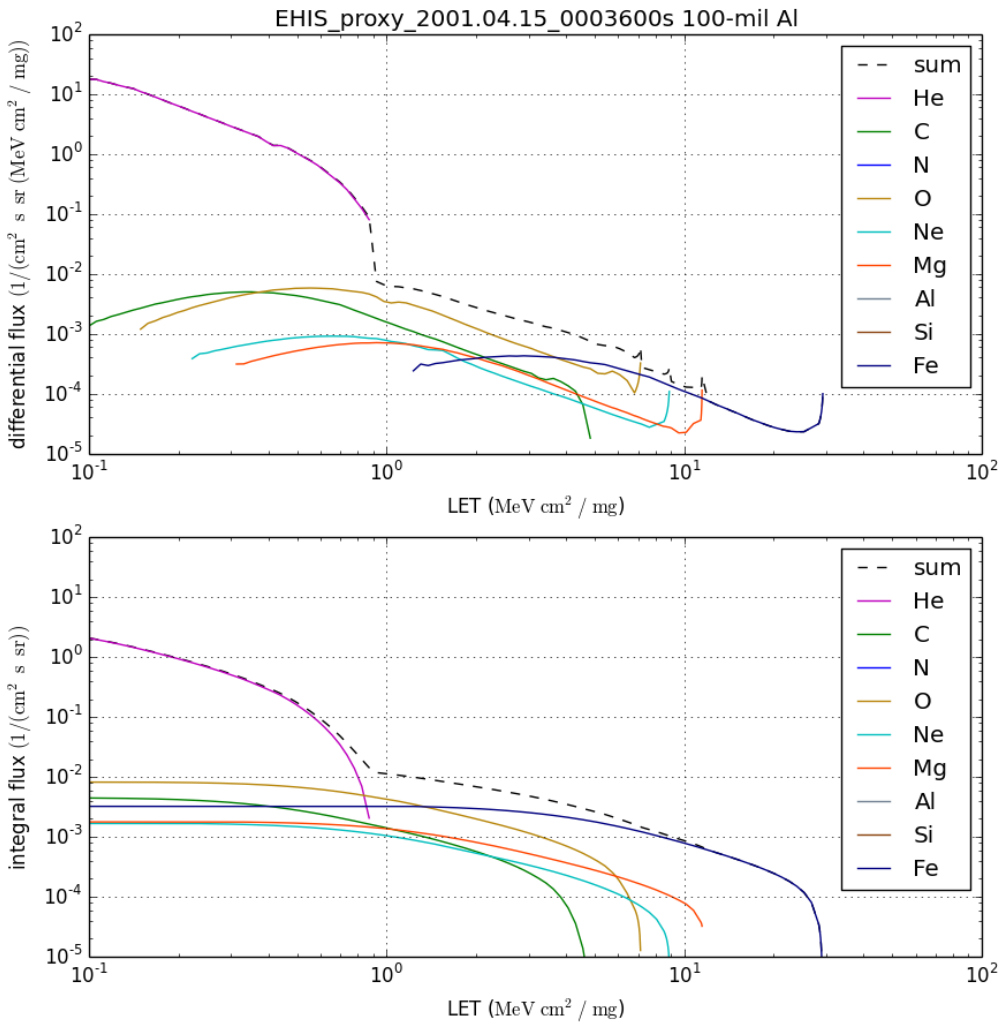


**Figure 24. Differential and integral LET spectra in silicon for the 15 April 2001 SEP event, under 100 mil Al shielding, assuming a 1-hour accumulation period. Six species are included; N, Al and Si are omitted since the fluxes are too low to register above the single count level in at least 2 energy channels.**

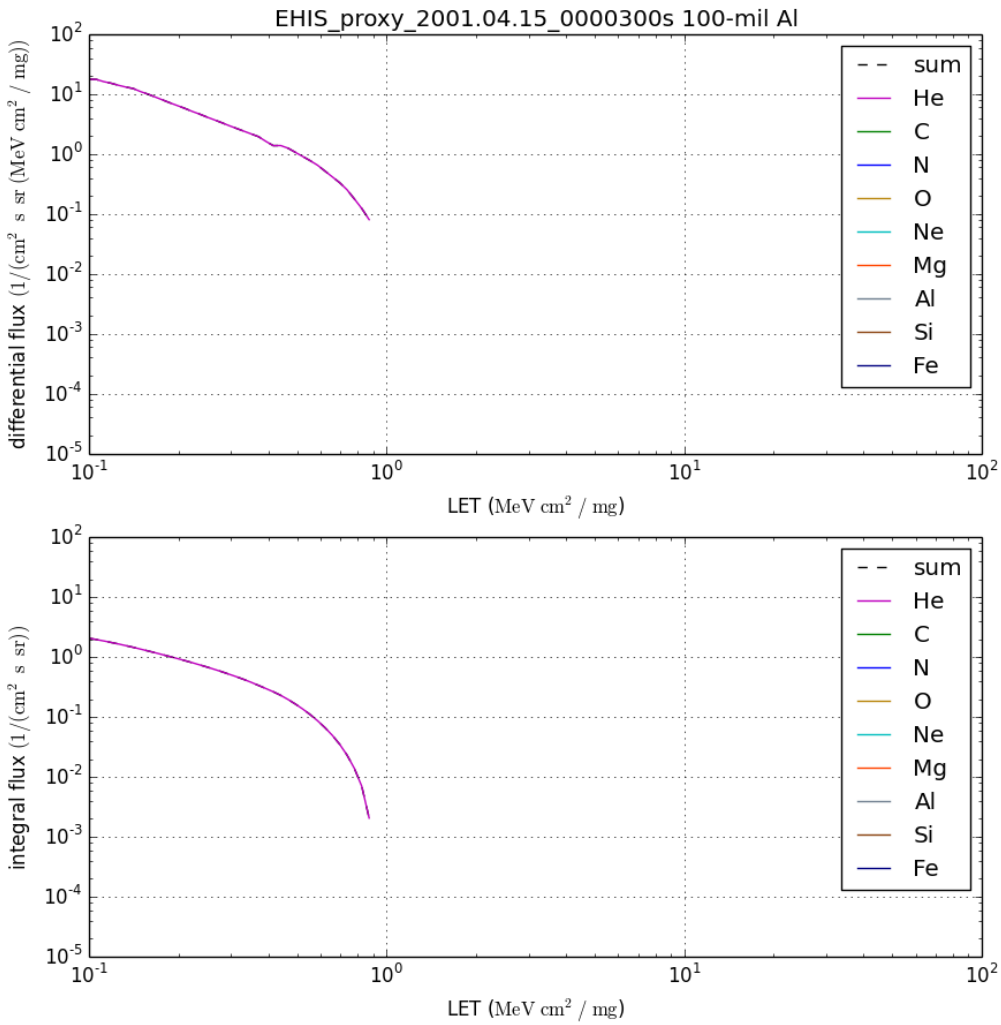


**Figure 25. Differential and integral LET spectra in silicon for the 15 April 2001 SEP event, under 100 mil Al shielding, assuming a 5-minute accumulation period. Only He is included; the other species are omitted since the fluxes are too low to register above the single count level in at least 2 energy channels.**

# 5.0 PRACTICAL CONSIDERATIONS

## 5.1 Numerical Computation Considerations

The implementation of the real-time algorithm requires linear fitting and linear interpolation routines. The linear interpolation routines are from the NumPy module while the linear fitting routine follows the theory in Press et al. [1988, p. 524] and is the same as that used in the rate-of-rise code.

## 5.2 Programming and Procedural Considerations

LUTs are generated from results of Monte Carlo (TRIM) analyses using custom IDL routines, including the spline coefficient generation used to calculate dE/dL. The real-time code has been developed in Python, consisting in two files, one containing the main program and one containing a custom library of functions for LET.

## 5.3 Quality Assessment and Diagnostics

In every 5-minute report, the EHIS spectral points ingested by the algorithm will be flagged: 1 if large enough to be used in the power law fit, 0 otherwise (below the background level). This information will indicate the maximum LET that could be observed in a given interval.

## 5.4 Exception Handling

If only one valid spectral point is available for a given heavy ion species, the power law fit cannot be performed and the species is not included in the LET calculation. If all EHIS heavy ion fluxes in a 5-minute L1b data record are “upper limit” values (for example, outside SEP events), the only output is the quality assessment of the number of EHIS spectral points per species that were fit by the power law, which will be all zeroes.

## 5.5 Algorithm Validation

Following GOES-R launch, the LET algorithm cannot be validated until the EHIS L1b fluxes have been validated. Validation requires SEP events. If GOES-R launches other than at the peak of a solar cycle like Solar Cycle 23, it is possible that there may be no strong SEP events during PLT. Therefore, it may only be possible to validate the LET algorithm (as well as the L1b fluxes) during post-launch test (PLT) in a retrospective mode that evaluates weak SEP or galactic cosmic ray fluxes derived from L0 counts averaged over a long period such as an event duration or a Bartels 27-day solar rotation.

## 6.0 ASSUMPTIONS AND LIMITATIONS

### 6.1 Constants to be Re-evaluated During Cal/Val

Currently, there are no constants to be re-evaluated during cal/val. The number of shielding thicknesses (currently 3) and the number of species for which LUTs are constructed (currently 9) may be changed as a result of evaluations of the EHIS fluxes during a SEP event.

### 6.2 Input and Output File Contents and Formats

See Table 1 and Table 3 for assumed contents of the input and output files. They will be netCDF4 files.

### 6.3 Performance

Algorithm development by the Space Weather Algorithm Team assumes that the EHIS instrument meets the performance requirements outlined in the GOES-R MRD and SEISS PORD. A key parameter to be determined during PLT is the flux level at which upper limits are typically reported (by species and energy).

### 6.4 Pre-Planned Product Improvements

If the validity range of this algorithm is extended to >500 mil Al shielding thicknesses, nuclear fragmentation will have to be accounted for. This will require using a model in place of TRIM to generate the transport look-up tables. The candidate model for this is FLUKA [Ferrari et al., 2005; Battistoni et al., 2007], which is used by the Space Radiation Analysis Group at Johnson Space Center. It was also used by the University of New Hampshire to model the EHIS. An algorithm modification, involving new LUTs, will be needed to account for the fragmentation results.

Based on the LET of helium up to the maximum EHIS energy (Figure 2), the LET range of this algorithm can be extended from 0.1 MeV $cm^2$ $mg^{-1}$ down to 0.01 MeV $cm^2$ $mg^{-1}$ by regenerating the look-up tables.

## 7.0 REFERENCES

Adams, J. H., Jr. (1983), The variability of single event upset rates in the natural environment, *IEEE Trans. Nuclear Sci., NS-30*, 4475-4480.

Badavi, F. F., J. W. Wilson, and A. Hunter (2005), Numerical study of the generation of linear energy transfer spectra for space radiation applications, *NASA TP-2005-213941*.

Battistoni, G., S. Muraro, P.R. Sala, F. Cerutti, A. Ferrari, S. Roesler, A. Fassò, and J. Ranft (2007), The FLUKA code: Description and benchmarking, Proceedings of the Hadronic Shower Simulation Workshop 2006, Fermilab 6--8 September 2006, M. Albrow, R. Raja eds., *AIP Conference Proceeding 896*, 31-49.

Bharath, R., J. V. Rodriguez, J. C. Green, and W. F. Denig (2003), Development of a proxy data set for the Energetic Heavy Ion Sensor (EHIS) in the GOES-R Space Environment In-situ Suite (SEISS), paper 296, *Ninth Annual Symposium on Future Operational Environmental Satellite Systems*, American Meteorological Society, January 5-10, 2013, Austin. (https://ams.confex.com/ams/93Annual/webprogram/Paper216161.html)

Bodeau, M. (2010), High energy electron climatology that supports deep charging risk assessment in GEO, 48th AIAA Aerospace Sciences Meeting, AIAA 2010-1608.

Cayton, T. E., and M. Tuszewski (2005), Improved electron fluxes from the synchronous orbit particle analyzer, *Space Weather, 3,* S11B05, doi:10.1029/2005SW000150.

Connell, J. J, C. Lopate, and R.B. McKibben (2001), The angle detecting inclined sensors (ADIS) system: measuring particle angles of incidence without position sensing detectors, *Nuclear Instruments and Methods in Physics Research A, 457*, 220-229.

Connell, J. J, C. Lopate, R.B. McKibben, and A. Enman (2007), Accelerator test of an angle detecting inclined sensor (ADIS) prototype with beams of $^{48}$Ca and fragments, *Nuclear Instruments and Methods in Physics Research A, 570*, 399-413.

Evans, D. S., and M. S. Greer (2000), Polar Orbiting Environmental Satellite Space Environment Monitor – 2: Instrument Descriptions and Archive Data Documentation, *NOAA Technical Memorandum*, OAR SEC-93.

Ferrari, A., P.R. Sala, A. Fassò, and J. Ranft (2005), FLUKA: a multi-particle transport code, CERN-2005-10, INFN/TC_05/11, SLAC-R-773.

Geissel, H., H. Weick, C. Scheidenberger, R. Bimbot, and D. Gardès (2002), Experimental studies of heavy-ion slowing down in matter, *Nuclear Instruments and Methods in Physics Research B, 195*, 3–54.

Hanser, F. A. (2011), EPS/HEPAD calibration and data handbook, *Tech. Rep. GOESN-ENG-048D*, Assurance Technol. Corp., Carlisle, Mass.

Heinrich, W. (1977), Calculation of LET-spectra of heavy cosmic ray nuclei at various absorber depths, *Radiation Effects, 34,* 143-148.

ICRU (2011), Fundamental quantities and units for ionizing radiation (Revised), ICRU Report No. 85, *Journal of the ICRU, 11*, the International Commission on Radiation Units and Measurements.

Jun, I., M. A. Xapsos, S. R. Messenger, E. A. Burke, R. J. Walters, G. P. Summers, and T. Jordan (2003), Proton nonionizing energy loss (NIEL) for device applications, *IEEE Trans. Nuclear Sci., 50*, 1924-1928.

Mazur, J. E. (2002), Summary report, workshop on energetic particle measurements for the GOES R+ satellites, October 28-29, 2002, Boulder, Colorado.

Paul, H. (2006), A comparison of recent stopping power tables for light and medium-heavy ions with experimental data, and applications to radiotherapy dosimetry, *Nucl. Instrum. Methods B,* 247, 166.

Paul, H., and A. Schinner (2005), Judging the reliability of stopping power tables and programs for protons and alpha particles using statistical methods, *Nucl. Instr. Methods B, 227,* 461

Press, W. H., B. P. Flannery, S. A. Teukolsky, and W. T. Vetterling (1988), *Numerical Recipes in C: The Art of Scientific Computing*, Cambridge University Press.

Raben, V.J., D. S. Evans, H. H. Sauer, S. R. Rahm, and M. Huynh (1995), TIROS/NOAA satellite space environment monitor data archive documentation: 1995 update. *NOAA Technical Memorandum*, ERL SEL-86.

Sigmund, P. (2004), *Stopping of Heavy Ions: a Theoretical Approach*, Springer Tracts in Modern Physics, v. 204.

Sørensen, A. H. (2003), Stopping of relativistic heavy ions; the pair production and bremsstrahlung channels, *Application of Accelerators in Research and Industry, 17th International Conference*, AIP Conference Publication 680, 102-105.

Stone, E. C., et al. (1998), The Solar Isotope Spectrometer for the Advanced Composition Explorer, *Space Sci. Rev., 86,* 357-408.

Tylka, Allan J., James H. Adams Jr, Paul R. Boberg, Buddy Brownstein, William F. Dietrich, Erwin O. Flueckiger, Edward L. Petersen, Margaret A. Shea, Don F. Smart, and Edward C. Smith (1997), CREME96: A revision of the cosmic ray effects on micro-electronics code, *IEEE Trans. Nuclear Science, 44,* 2150-2160.

Zeitlin, C., S. Guetersloh, L. Heilbronn, J. Miller, N. Elkhayari, A. Empl, M. LeBourgeois, B. W. Mayes, L. Pinsky, M. Christl and E. Kuznetsov (2008), Shielding experiments with high-energy heavy ionsfor spaceflight applications, *New Journal of Physics, 10,* 075007, 20 pp.

Ziegler, J. F., J. P. Biersack, and M. D. Ziegler (2008), *SRIM: The Stopping and Range of Ions in Matter*, version 7, www.SRIM.org.

## APPENDIX A. REQUIREMENTS.

The LET algorithm has the following requirements:

*General*

20.01.02 The algorithm shall operate at a cadence of 5 minutes for Event Detection and Linear Energy Transfer and 1 minute for Rate-of-Rise.

20.01.03 The algorithm shall perform all operations in less than 30 seconds.

*Algorithm Inputs*

20.02.02 The Linear Energy Transfer algorithm shall ingest the L1b 5-minute EHIS heavy ion fluxes.

*Processing*

20.03.13 The algorithm shall calculate 0.1 - 30 MeV $cm^2$ $mg^{-1}$ total (summed over species) linear energy transfer (LET) differential spectra [$cm^{-2}$ $s^{-1}$ $sr^{-1}$ (MeV $cm^2$ $mg^{-1}$)$^{-1}$] from EHIS energy spectra.

20.03.14 The algorithm shall calculate 0.1 - 30 MeV $cm^2$ $mg^{-1}$ total (summed over species) linear energy transfer (LET) integral spectra [$cm^{-2}$ $s^{-1}$ $sr^{-1}$] from EHIS energy spectra.

20.03.15 The algorithm shall calculate LET spectra for Silicon behind 50, 100, and 500 mils of Aluminum.

*Algorithm Outputs*

20.04.08 The algorithm shall produce LET spectra at a 5-minute cadence from input L1b fluxes that are not reported as an upper limit in at least two of five energy channels.

*Exception Handling*

See 20.04.08.

*Ancillary Data*

20.06.01 The algorithm shall not ingest any ancillary data.

## APPENDIX B. UNITS OF LET AND SHIELDING

Various units are used in the literature to describe shielding thickness. This variety also results in different units used to describe LET. The purpose of this appendix is to provide a reference for these unit conversions.

Since aluminum is a common spacecraft structural material, shielding is typically expressed in equivalent thickness of aluminum, even if it is not actually aluminum.

The thickness of shielding is commonly given in thousandths of an inch, or mils. It is often also given, sometimes in the same document [e.g., Bodeau, 2010] in terms of millimeters (mm).

$$1 \text{ inch} = 1000 \text{ mils} = 2.54 \text{ cm}$$

Shielding is also specified in terms of an areal density (g $cm^{-2}$), which is the product of the mass density of aluminum (2.702 g $cm^{-3}$) and the shielding thickness in centimeters (cm). More directly, the conversion factor is 145.7 mil/(g $cm^{-2}$).

$$1000 \text{ mils Al} = 6.86 \text{ g cm}^{-2}$$

For illustrative purposes, Table 4 lists selected thicknesses, including those of NOAA dome detector or dosimeter moderators, in ascending order of equivalent aluminum thickness. The SEM-1 thicknesses are from Raben et al. [1995]. The SEM-2 thicknesses are from Evans and Greer [2000]. The GOES EPEAD thicknesses are from Hanser [2011].

Reflecting the alternatives of expressing shielding in terms of thickness or density, LET is expressed in terms of energy lost per unit distance (e.g., keV/μm or MeV/mm, which are equivalent), or in terms of energy lost per unit distance per unit density of the target material (e.g., MeV $cm^2$ $mg^{-1}$). We use the latter (note the use of milligrams). To convert from keV/μm to MeV $cm^2$ $mg^{-1}$, multiply by $2.3211 \times 10^2$ [Ziegler et al., 2008].

**Table 4. Selected shielding or moderator thicknesses in terms of areal density and equivalent thickness of aluminum.**

| Source | Specified Shielding / Moderator | g $cm^{-2}$ | mil Al |
|---|---|---|---|
| GOES EPEAD D3 | 0.123 g $cm^{-2}$ Al | 0.123 | 18 |
| SEM-1 MEPED P6 | 0.127 cm Al | 0.343 | **50** |
| SEM-2 MEPED P6 | 0.137 cm Al | 0.370 | 54 |
| GOES-R MPS-HI DOS1 | 100 mil Al | 0.686 | **100** |
| NASA-HDBK-4002 | 110 mil Al in GEO vs. electrons | 0.755 | 110 |

| **Source** | **Specified Shielding / Moderator** | **g cm$^{-2}$** | **mil Al** |
|---|---|---|---|
| GOES-R MPS-HI DOS2 | 200 mil Al | 1.373 | 200 |
| GOES EPEAD D4 | 1.57 g cm$^{-2}$ Al | 1.570 | 229 |
| SEM-2 MEPED P7 | 0.213 cm Cu | 1.908 | 278 |
| this algorithm | 500 mil Al | 3.432 | **500** |
| SEM-1 MEPED P8 | 0.218 cm W | 4.197 | 611 |
| SEM-1 MEPED P7 | 0.584 cm Cu | 5.233 | 762 |
| GOES EPEAD D5 | 8.0 g cm$^{-2}$ Cu | 8.000 | 1166 |
| SEM-2 MEPED P8 | 0.457 cm W | 8.797 | 1282 |
| SEM-2 MEPED P9 | 1.496 cm W | 28.798 | 4196 |

Al = aluminum, Cu = copper, W = tungsten